Vol. 11 • No. 17 • September 4 • 2023

www.advopticalmat.de

ADVANCED OPTICAL MATERIALS

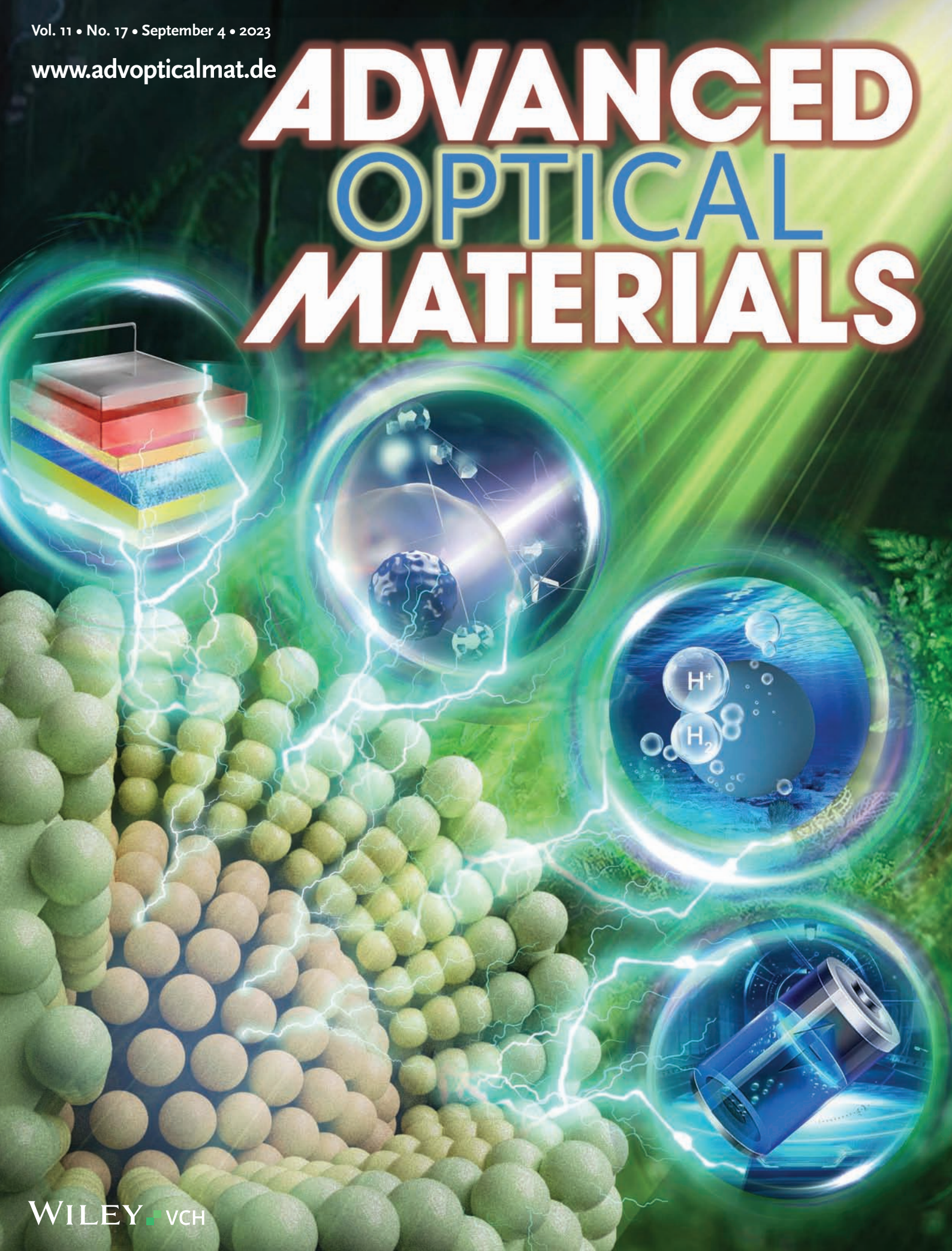

WILEY VCH

Check for updates

ADVANCED OPTICAL MATERIALS
www.advopticalmat.de

InP Semiconductor Nanocrystals: Synthesis, Optical Properties, and Applications

Huan Liu, Peixian Chen, Yanyan Cui, Yang Gao, Jiaji Cheng, Tingchao He, and Rui Chen**

As the most promising candidate for luminescent semiconductor materials in the future environmentally friendly society, InP nanocrystals (NCs) have attracted strong attention in the past decade. Tremendous efforts have been devoted to address the unstable and poor optical properties of InP NCs for practical applications. An extensive and in-depth summary of existing literatures can not only provide an important reference for further optimizing of the optical properties of InP NCs, but also lay a foundation for subsequent related applications. In this review, the methods for the synthesis with different P sources and different ZnE (E = Se, S) shells are briefly summarized. The research progress in the optical properties investigation of InP/ZnE and InP/ZnE/ZnE NCs, including absorption, fluorescence, carrier dynamics, and nonlinear optics, are summarized. The relevant applications based on InP/ZnE and InP/ZnE/ZnE NCs are also presented, ranging from light emitting diodes, bioimaging, and solar cells to photocatalytic hydrogen production.

1. Introduction

Semiconductor nanocrystals (NCs) with unique optical properties have attracted intensive attention as excellent materials for laser, solar cell, fluorescent probe, photodetection, etc.[1–4] Due to the quantum confinement effect, semiconductor NCs exhibit broad band absorption, narrow emission, continuously tunable emission wavelength, and high photoluminescence quantum yields (PLQY).[5,6] As a result, numerous practical applications based on semiconductor NCs, such as light emitting diode (LED) and bioimaging, have been achieved with exciting achievements in the past decades.[1,7] Up to date, these applications are mainly based on Cd/Pb-based NCs. Unfortunately, Cd/Pd is harmful to human body,[8,9] so relevant applications will be limited in the future green-friendly environment. Alternatively, environment-friendly semiconductor NCs, such as InP, $CuInS_2$, and ZnInS/ZnS NCs, have shown excellent development opportunities due to their low toxicity.[10–12] Among them, InP NCs are considered as the most promising candidates to replace Cd/Pb-based NCs due to their advanced optical properties.[13]

Compared with Cd/Pb-based NCs, InP NCs have received less attention due to their complicate synthesis. InP NCs had been synthesized by Mićić et al. in 1994 for the first time. The numerous surface defects in InP NCs make it difficult to study their electrical and optical properties.[14] To address this problem, great efforts have been devoted in the past two decades to find suitable phosphorus (P) sources and then grow ZnS, ZnSe as shell layers to improve quality of InP NCs.[15–17] Up to now, P sources like tris(trimethylsilyl)phosphine ($(TMS)_3P$) and tris(dimethylamino)phosphine ($(DMA)_3P$) have been used for the synthesis of InP/ZnE and InP/ZnE/ZnE (E = Se/S) NCs, and optical materials with a full width at half maximum (FWHM) of 37 nm and a PLQY of 95% have been sucessfully achieved.[18,19] The optical properties of InP NCs are affected by the core size. In addition, the emission wavelengths of InP NCs can be modulated from visible to near-infrared (NIR) region through changing of ZnS or ZnSe shells on InP core.[13] The defects on the InP core can be efficiently passivated and the PLQY can be improved significantly.

InP NCs have recently been synthesized through various methods and then applied to LEDs, bioimaging, and other fields.[16,20–25] The device performance based on InP NCs is comparable to Cd/Pb-based NCs and even better in some aspects. To expand the potential application of InP NCs, a systematic summary of the InP NCs in terms of synthesis, optical properties, and applications is crucial. Although there are some reviews about the synthesis and application of InP NCs, the summary on their optical properties is currently lacking, which is not beneficial for optimizing the application of InP NCs.[26–29]

In this review, the synthesis methods of InP NCs were first discussed. The optical properties of InP NCs, including absorption, fluorescence, carrier dynamics, Auger recombination, and nonlinear optics, are then systematically summarized. After that,

H. Liu, R. Chen
Department of Electrical and Electronic Engineering
Southern University of Science and Technology
Shenzhen 518055, P. R. China
E-mail: chenr@sustech.edu.cn

H. Liu, P. Chen, Y. Cui, Y. Gao, T. He
Key Laboratory of Optoelectronic Devices and Systems of Ministry of Education and Guangdong Province, College of Physics and Optoelectronic Engineering
Shenzhen University
Shenzhen 518060, P. R. China
E-mail: tche@szu.edu.cn

P. Chen, J. Cheng
School of Materials Science and Engineering
Hubei University
Wuhan 430062, P. R. China

The ORCID identification number(s) for the author(s) of this article can be found under https://doi.org/10.1002/adom.202300425

DOI: 10.1002/adom.202300425

 © 2023 Wiley-VCH GmbH

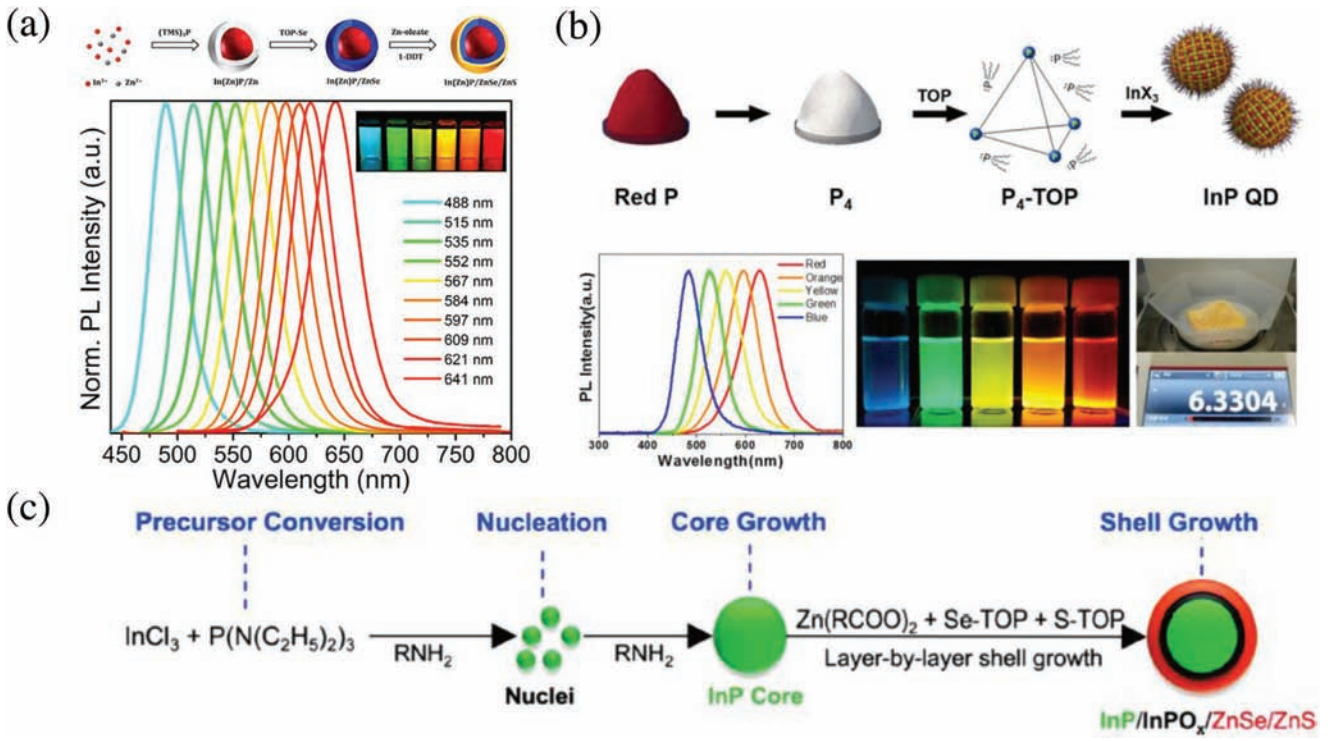

Figure 1. a) InP/ZnSe/ZnS NCs with luminescence emission in the range of 488–641 nm synthesized by $(TMS)_3P$ as a P source. Reproduced with permission.[13] Copyright 201□, American Chemical Society. b) Schematic diagram of the synthesis process of InP NCs by using P_4 as a P source. Reproduced with permission.[15] Copyright 201□, American Chemical Society. c) Typical synthesis process of InP/ZnSe/ZnS NCs. Reproduced with permission.[30] Copyright 2020, American Chemical Society.

an overview of the applications of InP NCs is provided, including LEDs, bioimaging and others. Finally, we prospect the potential research directions of InP NCs in future.

2. Synthesis of InP NCs

InP NCs with good crystallinity were first synthesized by Mićić et al. using chloroindium oxalate and $(TMS)_3P$ as raw materials in 1994.[14] However, due to the long reaction time, the InP NCs encapsulated by trioctylphosphineoxide (TOPO) have a poor size distribution, resulting in an obscure absorption peak. This problem was resolved by Adam in 1996 using selective precipitation to obtain highly crystalline, monodisperse InP NCs.[30] More importantly, the quantum confinement effect of InP NCs was demonstrated for the first time. The obtained InP NCs have almost no fluorescence because a large number of defects exist on the surface due to the high reactivity of the P source. At the same time, the high reactivity $(TMS)_3P$ not only leads to inhomogeneous size distribution of InP NCs but also generates harmful gases.[29] However, InP NCs prepared with $(TMS)_3P$ can exhibit bright visible NIR emission after being deposited by zinc sulfides (**Figure 1**a).[13] In recent years, the cheap and safe $(DMA)_3P$ has been chosen to gradually replace $(TMS)_3P$, because the InP synthesized based on $(DMA)_3P$ has shown comparable optical properties.[18,31] The use of $(DMA)_3P$ has greatly facilitated the study of InP NCs due to the complexity of $(TMS)_3P$. Recently, ultrahigh quality InP NCs with 37 nm FWHM and 97% PLQY were synthesized using $(DMA)_3P$ as a P source by Yang et al.[18] Briefly, indium halide, zinc halide, and 12 mL of oleylamine (OLA) were mixed in a three-neck flask and degassed at 120 °C for 60 min and then heated to 180 °C under a nitrogen atmosphere. Subsequently, $(DMA)_3P$ dissolved in trioctylphosphine (TOP) was injected rapidly at 180 °C and maintained for 2 min for the growth of InP.[18,31] Similar InP synthesis methods can be found in other literatures.[11,32–34] The obtained InP NCs have a large number of defects on the surface which leads to fluorescence quenching. Moreover, the oxide layers result in size inhomogeneity of InP NCs. The same deficiency exists in InP NCs synthesized from other P sources.[15,17] On the other hand, white phosphorus can also be used as a P source for the synthesis of InP NCs because of the similar bond energy of P–Si in $(TMS)_3P$.[15,30] A schematic diagram of the synthesis process of InP NCs employing white phosphorus is shown in Figure 1b. In the work of Park and coworkers, red phosphorus was phase transformed, predissolved in TOP to obtain P_4, and subsequently injected into the In precursor to obtain InP NCs.[15] Similarly, blue to red emitting InP NCs were obtained after the growth of ZnE (E = S, Se) shells. Recently, Zhao et al. utilized a new P source (NaOCP) to synthesize InP/ZnSe/ZnS NCs, which shown emission in the 456–620 nm with an external quantum efficiency (EQE) of 13.6% in the red band.[16] Other P sources such as PH_3 and PCI_3 have also been used for the synthesis of InP NCs.[17,35] However, those P sources are highly toxic and pose a challenge to the synthesis of InP NCs. Although a variety of P precursors have been developed, the most commonly used P precursors include $(TMS)_3P$ and $(DMA)_3P$, and the synthesized InP NCs exhibit narrow FWHM,

© 2023 Wiley-VCH GmbH

high PLQY, and high stability after being coated by other semiconductor shells.

For bare InP NCs, their dismal optical properties stemming from the presence of dangling bonds and oxide layers on the surface have been significantly improved upon epitaxial growth of a wide bandgap shell layer. In 2001, InP NCs encapsulated by wide bandgap ZnS were synthesized for the first time by Weller et al.[36] The reduction of surface defects leads to a decrease of its surface trap state emission and an improved band edge emission efficiency. The absorption and fluorescence of the InP/ZnS heterojunction underwent a slight redshift relative to the InP core. In addition, bare InP changes from almost no luminescence to a PLQY of 23%. During the synthesis of InP/ZnS NCs, adding zinc halide to the mixture of indium halide and OLA before growing InP not only serves as a Zn precursor but also improves the uniformity of InP size. After the injection of P precursors to form the InP core, 1-dodecanethiol (DDT), or mixed sulfur powder/TOP is injected to form the ZnS shell.[33,34] The synthesis of InP/ZnSe is similar to that of InP/ZnS.[37] Although the optical properties of InP had been enhanced remarkably after coating the ZnS and ZnSe shells, the broad emission spectra and weak PLQY still lagged behind those of Cd/Pb-based NCs until InP/ZnSe/ZnS NCs with a PLQY of 95% were synthesized by Peng et al.[19] InP/ZnSe/ZnS NCs with comparable optical properties to CdSe were synthesized by high-temperature injection of $(TMS)_3P$ or $(DMA)_3P$, Se-TOP and S-TOP as P, Se-, and S-sources, respectively.[38] In addition, alternate injection of Zn and Se/S precursor can achieve ZnSe/ZnS shell layer with controllable thickness.[13] The facile InP/ZnSe/ZnS NCs synthesis process is shown in Figure 1c.[39]

Introducing transition metal elements into NCs to form dopants is one of the methods to modify the optical properties of NCs. The Cu-doped InP/ZnSe core/shell NCs were first studied by Peng et al. in 2009, by exploring the chemical conditions associated with the synthesis, such as shell thickness, doping concentration, and reaction temperature.[40] The one-pot synthesis of Cu-doped InP/ZnSe can be simply described by three stages, namely the formation of InP core, the injection of Cu precursor solution thereafter, and the growth of ZnSe shells by sequential ion layer adsorption reaction (SILAR). The emission of Cu-doped InP/ZnSe can be tuned from 630 to 1100 nm by the doping concentration, shell thickness, and reaction temperature. Besides, Mn had been used as a dopant for the synthesis of Mn-doped InP/ZnS NCs by Guo et al. in 2018.[32] Unlike the synthesis of Cu-doped InP/ZnSe, the starting Mn precursor was first mixed with zinc and indium precursors and heated, which was followed by the injection of P and S precursor to form the InP core and ZnS shell layer, respectively. Similarly, the optical properties of InP NCs can be adjusted by doping other metal elements such as Al, Ag, and Zn.[41–43]

3. Photophysical Properties of InP NCs

3.1. Absorption

It is known that the optical properties of semiconductor NCs are determined by their size which can be manipulated through the reaction temperature, reaction time and feed concentration during the synthesis process.[44] **Figure 2**a shows the UV–vis absorption spectra of InP NCs fabricated at different reaction times, where the first exciton absorption peak shifted from blue to the red with the increase of reaction time.[45] In addition, the higher temperature of the injected P precursor can form a bigger InP NCs. Dissimilar to CdSe NCs, the first exciton absorption peak of InP NCs can be adjusted by different type of halide ions. As shown in Figure 2b, green, orange, and red InP NCs were synthesized by changing the species of indium halide.[31,34,46] It is noted that the binding strength of amine to $InCI_3$ is greater than that of $InBr_3$ and InI_3, making $InCI_3$ easier to dissolve. Moreover, adsorption sites are easily accessible due to the smaller size of the chloride ions adsorbed on the surface of the InP which may result in a change of the surface reaction rate.[46] These two combined effects lead to the size change of InP NCs due to the influence of halide ions. Moreover, owing to narrow bandgap (1.35 eV) and large Bohr exciton radius (10 nm), the effect of size on the optical properties of InP is stronger than that of CdSe NCs (bandgap of 1.74 eV and bohr exciton radius of 5.4 nm).[47,48] As shown in Figure 2c, the change in InP volume for the same absorption spectral range is only half of the CdSe.[48] This indicates that the absorption properties of InP NCs will be easier to adjust by size than CdSe NCs.

Although the absorption peak of InP NCs can be well tuned through the size, a large number of nonradiative channels are need to be suppressed by growing wide bandgap materials such as ZnS or ZnSe on its surface. After the growth of ZnS or ZnSe shell on the surface of InP NCs, a type I electronic band structure will be formed. The first exciton absorption peaks of InP/ZnS and InP/ZnSe NCs will redshift by 60 and 120 meV, respectively (Figure 2d).[46] Due to the small conduction band offset between the InP and ZnSe, electron wave function will extend to the ZnSe shell, which leads to a large absorption peak redshift relative to ZnS.[37,46,49] Although the absorption properties of InP will not be seriously affected by ZnSe and ZnS, it was found in Dennis□recent work that comparable visible emission intensity from InP is achieved by adjusting the thickness of ZnSe to produce different molar extinction coefficients.[48] It should be noted that the definition of luminance is $B =$ $*\epsilon$, where is the PLQY and ϵ is the molar extinction coefficient. Moreover, the emission intensity of larger InP NCs is usually higher than that of small ones, because the molar extinction coefficient is proportional to the size of the NCs. This may explain why the EQE of LEDs based on red InP NCs is larger than the green and blue ones (**Table 1**). In addition, although the shell does not obviously shift the absorption peak of InP, the fluorescence intensity has changed significantly due to the passivation of surface defects. However, reabsorption effects were found to be caused by the small Stokes shifts and the broad fluorescence spectrum in InP NCs. This challenge can be safely eliminated by doping with transition metals. Similarly, the emission peak of InP NCs has changed apparently by dopant, but the dopant cannot change the absorption characteristics of InP NCs.[33,50] That□s because the dopant forms a new radiation recombination center in the energy level of InP/ZnE.

3.2. Fluorescence

An essential prerequisite for semiconductor NCs that can be used in optoelectronic devices and bioscience is that they exhibit

© 2023 Wiley-VCH GmbH

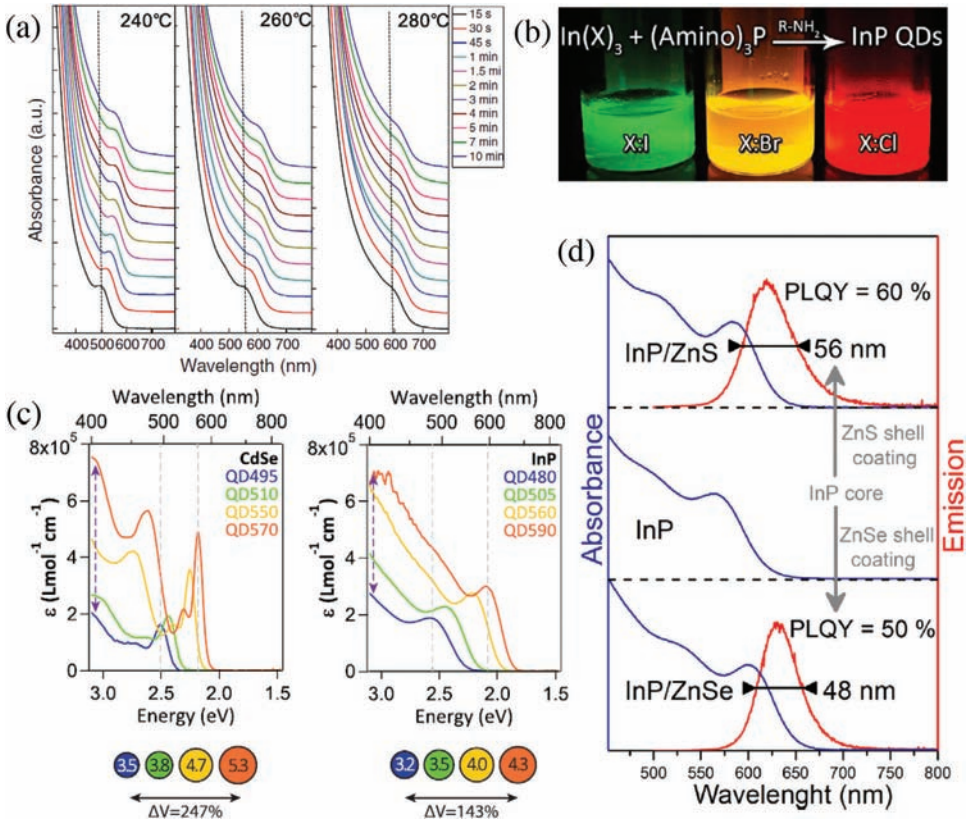

Figure 2. a) Absorption spectra of InP NCs at different reaction times and temperatures. Reproduced with permission.[45] Copyright 2013, Springer. b) InP colloidal NC solutions synthesized with different halides under UV light irradiation. Reproduced with permission.[46] Copyright 2015, American Chemical Society. c) The volume differences between InP and CdSe NCs in the same absorption range. Reproduced with permission.[48] Copyright 2021, American Chemical Society. d) Absorption and fluorescence spectra of InP, InP/ZnS, and InP/ZnSe NCs. Reproduced with permission.[46] Copyright 2015, American Chemical Society.

excellent fluorescence properties. However, InP NCs possess poor emission efficiency (less than 1%) and broad emission spectrum due to the presence of abundant defect states on the surface and poor size uniformity caused by oxide layers.[14,51,52] As shown in **Figure 3**a, the resultant InP NCs exhibit weak fluorescence with FWHM as big as 100 nm.[53] Etching surface defects from the InP NCs by HF is a meaningful method to enhance the luminescence properties until effective shell engineering is available. Arthur et al. demonstrated that InP NCs defects associated with deep red emission (above 850 nm) were eliminated, and room temperature PLQY was enhanced from 1% to 30% by HF etching.[54] In the study of Kim et al., the bare InP NCs etched by HF exhibit remarkably enhanced fluorescence intensity and stability, compared to the as-grown one, as shown in Figure 3b.[55] The PLQY elevation and fluorescence redshift of InP NCs treated by HF are due to the passivation of In dangling bonds on the surface of InP NCs.[55] Besides, HF was used to etch the oxide layer on the InP NCs surface, resulting in the enhanced fluorescence intensity.[51] However, the HF etching method is inadequate due to the instability of InP in air without a protective shell. As an alternative, effective surface passivation can be achieved by shell engineering rather than HF etching. For example, HF etching can only passivate hole defects on the surface of InP NCs, while ZnS shells can passivate both electron and hole defects, which was confirmed by comparing ultrafast carrier dynamics of HF and ZnS treatment of InP NCs.[56] Moreover, the PLQY of InP NCs passivated by ZnS is twice as high as the ones treated with HF (i.e., 40% vs 20%). The fluorescence lifetime of the former (49.4 ns) is also longer than the latter (32.4 ns).[56] For using a shell layer to passivate surface defects, typically, the possibility of interface defect formation is elevated by a larger lattice mismatch between the core and the shell. Interestingly, although the lattice mismatch of InP and ZnSe (3.4%) is smaller than that of InP and ZnS (7.6%), the PLQY obtained for InP/ZnS (60%) is higher than that of InP/ZnSe (50%) under the same growth conditions (Figure 2d).[46] Similar results has been observed by Jang et al.[37] The PLQY anomaly is thought to be originated from excitons confined in the InP core, due to the larger band offset between InP and ZnS relative to ZnSe. However, the FWHM of InP/ZnSe (39 nm) is smaller than that of InP/ZnS (50 nm), which can be ascribed to better uniformity due to the smaller lattice mismatch.[37]

Hence, to obtain InP NCs with narrower emission and higher PLQY, ZnSe was used as an intermediate layer to decrease the large lattice mismatch between InP and ZnS, which results in InP/ZnSe/ZnS multishell structures with comparable optical properties to CdSe/CdS. It should be noted that the formed InP/ZnSe/ZnS multishell structure still maintains type I electronic band structure due to the large band offset between the

© 2023 Wiley-VCH GmbH

Table 1. The optical parameter, P source, and EQE of InP-based NCs.

Sample	PL peak	PL FWHM	PLQY	PL Lifetime	P Source	EQE	Refs.
InP	5□0 nm	55 nm	<1%	N.A	$(TMS)_3P$	N.A[a)]	[123]
InP	522 nm	N.A	<1%	□.3 ns	NaCOP	N.A	[16]
InP	610 nm	60 nm	20%	N.A	PCl_3	N.A	[35]
InP-HF	≈630 nm	N.A	36%	68 ns	$(TMS)_3P$	N.A	[55]
Cu: InP	□3□ nm	N.A	0.8%	□14 ns	$(TMS)_3P$	N.A	[84]
InP/ZnS	5□0□□20 nm	50□65 nm	22%	N.A	PH_3	N.A	[1□]
InP/ZnS	530 nm	55 nm	60.1%	N.A	$(DMA)_3P$	0.223%	[124]
InP/ZnS	≈600 nm	56 nm	60%	N.A	$(TMS)_3P$	N.A	[46]
InP/ZnS	555 nm	60 nm	60%	5□.□ ns	P_4	N.A	[15]
InP/ZnSe	≈630 nm	48 nm	50%	N.A	$(TMS)_3P$	N.A	[46]
InP/ZnSe	585 nm	51 nm	43%	68 ns	$(TMS)_3P$	N.A	[□□]
InP/ZnSeS	520 nm	≈50 nm	80%	N.A	$(TMS)_3P$	3.46%	[110]
InP/ZnSeS	62□ nm	4□ nm	65%	25 ns	$(DMA)_3P$	N.A	[125]
Cu: InP/ZnSe	□□2 nm	N.A	5%	□36 ns	$(TMS)_3P$	N.A	[84]
Mn: InP/ZnS	51□ and 5□2 nm	N.A	15%	13 ns and 1.3 ms	$(DMA)_3P$	N.A	[33]
InP/ZnSe/ZnS	538 nm	38 nm	86%	N.A	$(TMS)_3P$	N.A	[6□]
InP/ZnSeS/ZnS	52□ nm	3□ nm	8□%	50 ns	$(DMA)_3P$	N.A	[15]
InP/ZnSe/ZnS	465 nm	42 nm	43%	N.A	NaCOP	1.4□%	[16]
InP/ZnS/ZnS	468 nm	4□ nm	40%	65.2 ns	$(DMA)_3P$	1.□%	[126]
InP/ZnSe/ZnS	≈535 nm	40 nm	8□%	□2 ns	$(TMS)_3P$	6.2%	[12□]
InP/ZnSe/ZnS	60□ nm	40 nm	□3%	51.□ ns	$(TMS)_3P$	6.6%	[38]
InP/ZnSe/ZnS	533 nm	36 nm	□□%	104.□8 ns	NaCOP	6.88%	[16]
InP/ZnSeS/ZnS	525 nm	45 nm	□5%	3□.04 ns	$(DMA)_3P$	□.06%	[31]
InP/ZnSeS/ZnS	525 nm	35 nm	□□%	□6.8 ns	$(DMA)_3P$	15.2%	[111]
InP/ZnSe/ZnS	618 nm	42 nm	□5%	N.A	$(TMS)_3P$	12.2%	[1□]
InP/ZnSe/ZnS	620 nm	52 nm	□5%	N.A	NaCOP	13.6%	[16]
InP/ZnSe/ZnS	630 nm	N.A	□4%	40 ns	$(TMS)_3P$	18.6%	[□0]
InP/ZnSe/ZnS	630 nm	35 nm	100%	34 ns	$(TMS)_3P$	21.4%	[60]
ZnSe/InP/ZnS	515□845 nm	□5□1□4 nm	36□13%	6□□132 ns	$(TMS)_3P$	N.A	[5□]

[a)] Not available.

conduction and valence bands of ZnSe (2.7 eV) and InP (1.35 eV) and ZnS (3.6 eV).[30,38] Such type I electronic band structure hinders surface-assisted relaxation processes and charge transfer to organic ligands, especially for the case of low energy excitation.[48] Through adjusting the size of InP and the thickness of ZnSe and ZnS, the InP/ZnSe/ZnS, tunable emission in the visible band can be obtained as shown in Figure 3c.[25] Except for the core–shell structure, the InP/ZnSeS core/alloy shell structure was introduced to reduce the lattice mismatch between the core and the shell and thus improve the fluorescence properties.[51,57] As shown in Figure 3d, the core/alloy shell structure shows less interfacial defects relative to the core–shell structure, and therefore superior fluorescence properties can be achieved.[58] Besides, the optical properties of InP NCs can also be tuned by designing the InP as an intermediate shell layer to obtain ZnSe/InP/ZnS NCs to form an anti-type I structure. Importantly, this structural design breaks the limits of InP emission which locates at visible wavelengths, and realized NIR emission which is critical for application in bioimaging.[59]

Moreover, the two passivation strategies can be combined. Pretreatment of the InP NCs core and subsequent shell engineering are applied together to modify the optical properties of InP NCs. In a recent study by Tseng et al., the HF-treated InP cores followed by the growth of $ZnSe_xS_{1-x}$ shell exhibited better optical properties compared to InP NCs without HF treatment.[51] Most of the defect states and oxide layers are presented in non-HF-treated InP and InP/ZnSeS NCs, while the samples with HF treatment almost defect free.[51] Similarly, in the work of Jang et al., the surface defects and oxide layers were eliminated by adding HF during the synthesis of InP NCs. With the subsequent growth of ZnSe and ZnS shell, the InP/ZnSe/ZnS NCs with a near-unified PLQY was obtained as a result of further passivation of the remaining defects on the InP surface. Emission with FWHM of 35 nm and an EQE of 21.4% were achieved in InP/ZnSe/ZnS NCs based LEDs.[60]

Besides HF etching and shell engineering, ion passivation has also been used to passivate surface defects to optimize the fluorescence properties of InP NCs. The work by Gamelin et al. confirmed that defects on the surface of InP NCs can be passivated not only by ZnSeS, but also by simple binding with F^-, Zn^{2+}, or Cd^{2+}. Based on the transient absorption spectroscopy (TAS) and time-resolved photoluminescence (TRPL) measurements, it

© 2023 Wiley-VCH GmbH

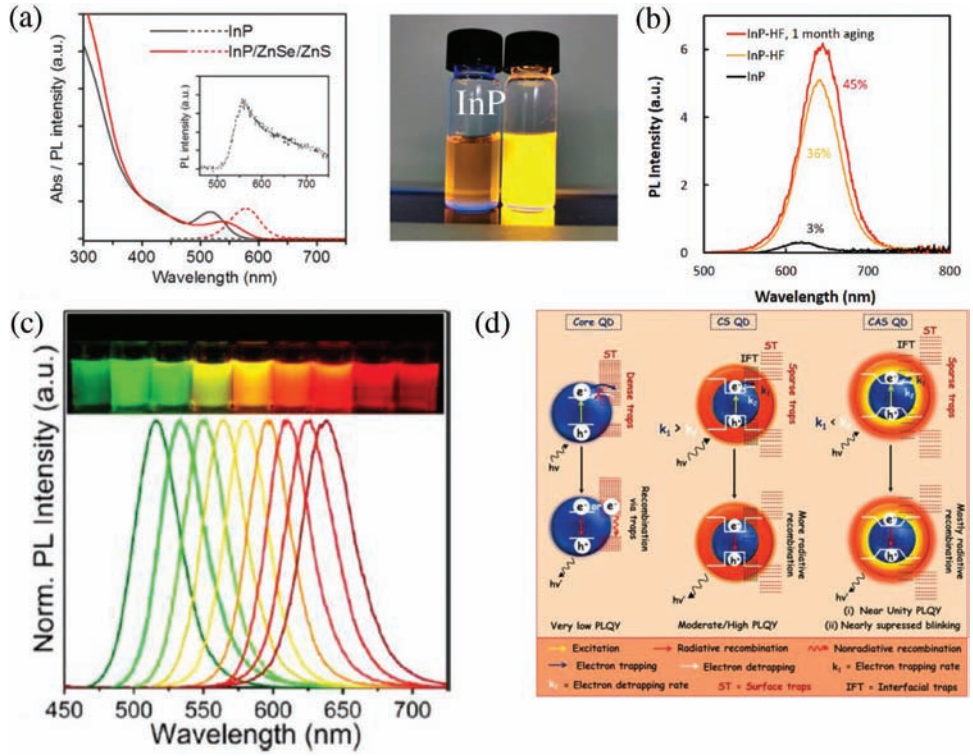

Figure 3. a) The absorption and PL spectra of InP and InP/ZnSe/ZnS NCs (Left), the PL spectrum of InP NCs (Inset), InP and InP/ZnSe/ZnS NCs colloidal solutions upon UV lamp irradiation (Right). Reproduced with permission.[53] Copyright 2020, American Chemical Society. b) PL spectra and PLQY before and after HF etching of InP NCs. Reproduced with permission.[55] Copyright 2018, American Chemical Society. c) InP/ZnSe/ZnS NCs solutions under UV lamp irradiation (Top) and PL spectrum of InP NCs with different core sizes (Bottom). Reproduced with permission.[25] Copyright 2018, American Chemical Society. d) Electronic structures, interfacial defect energy levels, and surface defect energy levels schematics of InP core, InP/ZnSe core/shell (CS) and InP/ZnSeS core/alloy□shell (CAS). Reproduced with permission.[58] Copyright 2022, American Chemical Society.

was confirmed that both electron and hole defects contribute to the nonradiative recombination induced by the surface defects in InP NCs.[61] The electronic defects can be partially suppressed by F and Zn^{2+}, while almost all of them are eliminated by Cd^{2+}. A straightforward result is presented in **Figure 4**a, where the PLQY of InP NCs bound with F , Zn^{2+}, and Cd^{2+} are 20%, 21%, and 54%, respectively. Furthermore, the PLQY of InP NCs bound with Cd^{2+} reaches ≈54%, while the PLQY of the as-grown InP NCs is less than 1%, indicating the electron and hole defects are in equal amounts on the InP NCs surface.[16,52] Also, their results confirm that ZnSeS as a passivation layer can partially passivate not only electron defects but also hole defects, which is consistent with the results of Lian et al.[56,61]

The fluorescence properties of InP NCs can also be tuned by doping with transition metal elements. Additional energy levels will be introduced by transition metal elements, which results in the formation of new emitting states through charge transfer or energy transfer. For example, Cu-doped InP/ZnSe NCs with emission wavelength ranging from 630 to 1100 nm were synthesized by Peng et al. by controlling the size of InP NCs, which greatly compensates for the deficiency of undoped InP NCs in the NIR emission band. The fluorescence spectra of doped and undoped InP NCs are shown in Figure 4b. The redshift and broadening of the PL spectra after doping were derived from the formation of new defect emission centers. In addition, the emission intensity of Cu ions can be adjusted by the doping concentration, which indicates the possibility that the dual-emission Cu-doped InP/ZnSe NCs can be used as a temperature detector.[62] More importantly, NIR emission has a longer penetration depth in biological tissues than visible light, which provides the possibility to realize the application of InP NCs composed of non-heavy elements in biosciences.[63,64] Although the undoped InP NCs with NIR emission can also be synthesized to form type II electronic band structure through CdSe as a shell, the Cd^{2+} can also be introduced at the same time.[65] Unlike Cu-doped InP, the emission of Mn ions is attributed to the energy transfer from the InP exciton.[33] Similarly, the Mn fluorescence intensity can be tuned by controlling the doping concentration. In the Mn-doped InP/ZnS NCs, the Mn emission intensity increases and the exciton peak redshifts with the increase of Mn doping concentration, as shown in Figure 4c.[32]

PLQY plays a crucial role in the optical properties of InP NCs. In order to have a convenient comparison, the optical properties of InP NCs including PL peak, PLQY, FWHM, EQE, P sources, and lifetime are summarized in Table 1. The PLQY of bare InP NCs is less than 1%, as a result of a large number of surface defects. As mentioned above, the PLQY of bare InP NCs etched by HF can reach 30%. The PLQY for InP NCs with shell-engineered passivation is variable but higher than the samples with HF etching. For ZnSe or ZnSeS coated InP NCs, the latter one has bigger PLQY due to the smaller lattice mismatch between ZnSeS and InP.[66] Although the lattice mismatch between InP

© 2023 Wiley-VCH GmbH

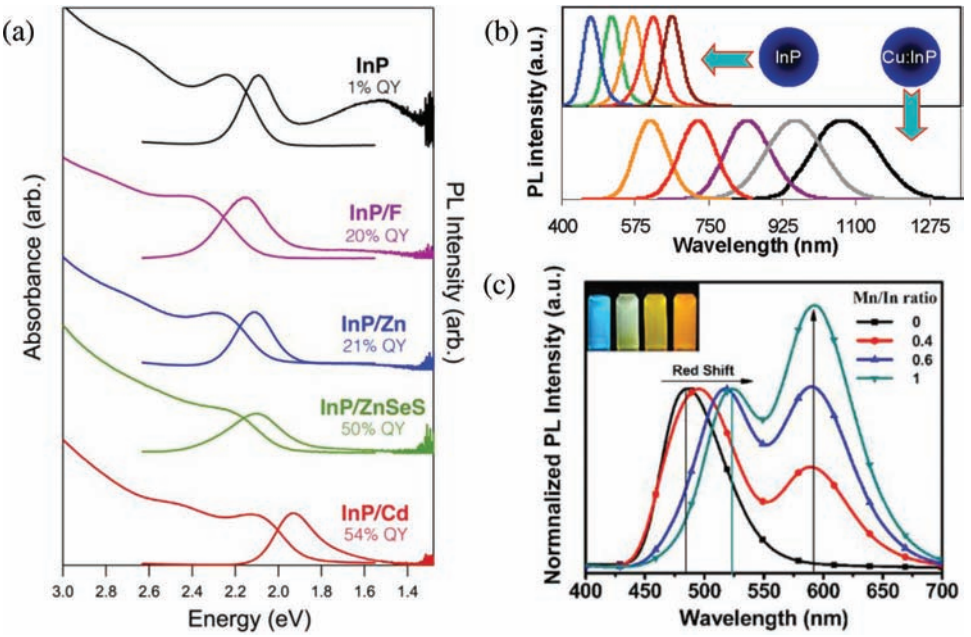

Figure 4. a) Absorption, PL spectra and PLQY of InP, InP/F, InP/Zn, InP/ZnSeS, InP/Cd NCs. Reproduced with permission.[61] Copyright 201□, American Chemical Society. b) The PL spectra of InP NCs (Top) and Cu-doped InP NCs (Bottom). Reproduced with permission.[62] Copyright 200□, American Chemical Society. c) PL spectra of InP NCs with di□erent Mn doping concentrations. Reproduced with permission.[32] Copyright 2021, Springer.

and ZnS is larger than that of ZnSe, the stronger exciton confinement effect leads to a higher PLQY of InP/ZnS relative to InP/ZnSe NCs.[46] The PLQY of InP/ZnSe/ZnS multishell structure is higher than that of InP/ZnSe and InP/ZnS NCs, and the FWHM is significantly narrowed.[31,37] On the other hand, the PLQY of InP NCs was found to increase with the increase of excitation wavelength.[48,67] Under higher energy excitation, the electrons and holes passed through the nonradiative defect states located in the upper part of the bandgap. As a result, the carriers will be captured by these defect states, which results in the low PLQY (**Figure 5**).[58] Some recent studies have shown that traps are In ions will enter the ZnSe shell to release tensile stress due to the radius of indium (152 pm) lager than zinc (148 pm). Therefore, shallow defects formed in the ZnSe shell might affect the PLQY of InP NCs.[19,68–70] Although some optical parameters of InP NCs are still slightly lower than those of CdSe NCs, the continuous improvement of optical properties over the last decade has confirmed that InP NCs will gradually replace CdSe NCs in various application fields.

The optical properties of semiconductor NCs will be affected by temperature.[71] Typically, the bandgap of semiconductor NCs shrinks with the increase of temperature, resulting in a redshift of the emission.[63] Beside the bandgap, temperature has effects on the emission band width, emission intensity, and decay time of semiconductor NCs.[72] Moreover, special emissions may only be observed at low temperatures, such as localized exciton emission.[73] In 2009, the temperature-dependent PL spectra were reported for four InP/ZnS NCs with different sizes by Zaag et al. Fluorescence redshift due to lattice expansion was observed in InP/ZnS NCs with the increase of temperature from 2 to 525 K (**Figure 6**a). Typically, the parameters of the bandgap shrinkage with temperature for semiconductor NCs can be obtained by fitting the experimental data with the following Varshni expression[74]

$$E_g(T) = E_g(0) + \alpha T^2 \quad (T + \beta) \tag{1}$$

where $E_g(0)$ is the bandgap of the material at 0 K, α is the temperature coefficient, and β is the material intrinsic coefficient. The value of α decreases with increasing size of InP/ZnS NCs, demonstrating that the fluorescence properties of InP/ZnS NCs with large size are less affected with temperature increasing. Unlike α, the values of β for all samples are consistent with the reported bulk material (β = 327 K). Furthermore, because the Varshni expression is an empirical formula obtained from the bulk material, the data in Figure 6a should be more accurately described by the following equation proposed by Chen et al.[75]

$$E_g(T) = E_g(0) \quad \frac{2S\langle\hbar\omega\rangle}{\exp\left(\langle\hbar\omega\rangle \quad K_B T\right) \quad 1} \tag{2}$$

Here, $E_g(0)$ is the bandgap at 0 K, S is the Huang–Rhys factor, $\hbar\omega$ is the average phonon energy, and K_B is the Boltzmann constant. According to the fitting results, it is found the bandgap of bigger InP/ZnS NCs is more temperature dependent. This is why fluorescence variation is more pronounced for the InP/ZnS NCs with smaller size as shown in Figure 6b.[76] The electron wave function of small InP/ZnS NCs will extend to the particle surface and generate radial electric field which increases exciton phonon coupling through the Fröhlich mechanism.[77] It is found that the spillover of the electron wave function depends on the size of the NCs. For smaller InP/ZnS NCs, more spillover of the wave function will result in stronger exciton phonon coupling and larger S. In addition, $E_g(0)$ also follows the same

© 2023 Wiley-VCH GmbH

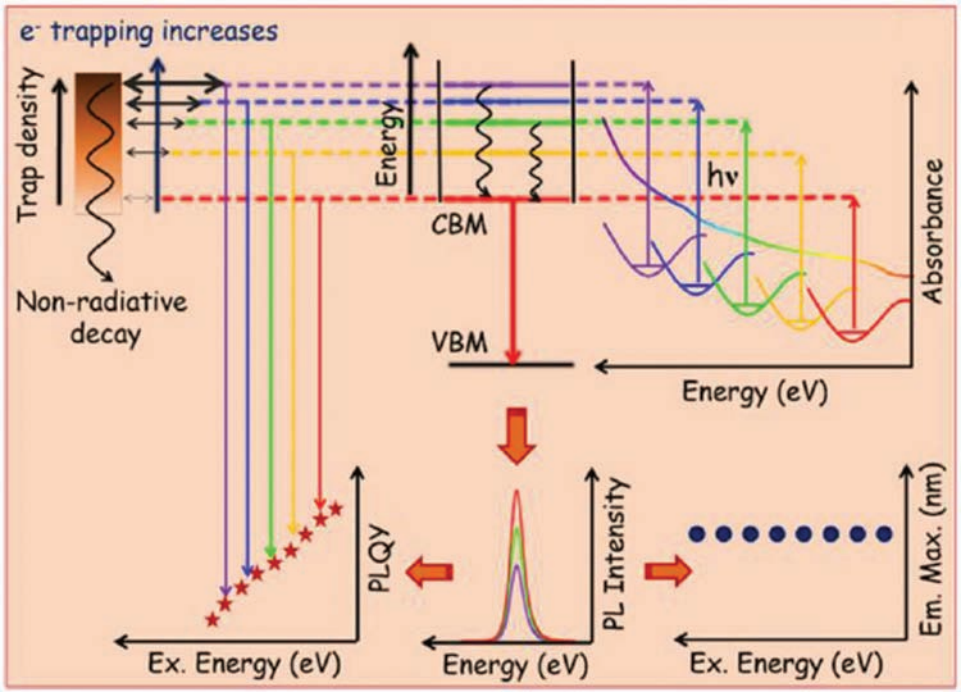

Figure 5. InP NCs excitation wavelength-dependent optical properties, including absorption, fluorescence, and PLQY. Reproduced with permission.[58] Copyright 2022, American Chemical Society.

trend as S due to quantum confinement effects.[77] The average phonon energy of the four size InP/ZnS NCs is about 23 meV, consistent with the result obtained by Wang et al. (22 meV).[77]

In addition to adjusting the bandgap of NCs, temperature also influences the emission linewidth of InP/ZnS NCs. The emission linewidth of NCs varies with temperature due to the combination of inhomogeneous and homogeneous broadening. The temperature dependent emission linewidth of InP/ZnS NCs in the range of 2–525 K is shown in Figure 6c. The results can be fitted by the following equation[72,76]

$$(T) = \ _{\text{inh}} + \sigma T + \ _{\text{LO}}\left(\exp\left(E_{\text{LO}} \ K_{\text{B}}T\right) \quad 1\right)^{1} \tag{3}$$

where $_{\text{inh}}$ is the inhomogeneous broadening, σ is the coupling coefficient between exciton and acoustic phonon, $_{\text{LO}}$ is the exciton-longitudinal optical (LO) phonon coupling strength, and E_{LO} is the phonon energy.[72,76] The inhomogeneous broadening is affected by the shape and component of the NCs, while the homogeneous broadening is affected by the exciton–phonon interaction. There is no obvious difference in the inhomogeneous broadening $_{\text{inh}}$ for the InP/ZnS NCs with different sizes. In contrast, the exciton-acoustic phonon coupling strength decreases with the size increase of the InP/ZnS NCs, because it is affected by the short-range interaction of potential energy.[77,78] For the exciton-LO phonon coupling strength, it exhibits an opposite trend due to long-range Fröhlich interaction which increases with the size increase of NCs.[79,80] The LO phonon energy E_{LO} obtained for InP/ZnS NCs with different sizes (≈40 meV) is similar to that of the InP bulk material (42.8 meV). The same experimental results can be found in the study of Wang et al. (≈41 meV).[77]

The effect of temperature on the emission intensity of InP NCs is also an interesting aspect. Usually, the emission intensity of NCs decreases with increasing temperature, which mainly ascribes to the nonradiative processes activated by temperature.[81,82] This is true for InP/ZnS NCs as shown in Figure 6d.[77] However, for Mn-doped InP/ZnS NCs, the excitonic emission intensity increases with increasing temperature, while the Mn emission intensity shows an opposite trend.[33] It is due to the fact that the energy transfer efficiency between the InP and Mn defect states decreases with increasing temperature. On the other hand, the effect of temperature on the charge transfer in the defect and neutral states is another important factor which will affect the InP/ZnS NCs fluorescence properties. The band tail emission of InP/ZnS NCs caused by traps has been observed at low temperatures, while it is not noticeable at room temperature.[37] The same phenomenon was also observed in InP/ZnSe NCs. However, this low-energy defect related emission is not observed in InP/ZnSe/ZnS NCs at low temperatures (Figure 6e), as a result of better passivation by multishells.[37]

3.3. Fluorescence Decay Process

The fluorescence decay time affected by radiative and nonradiative recombination is also an important physical parameter to characterize the photophysical properties of InP NCs. The average fluorescence lifetimes from different InP NCs are summarized in Table 1. In general, the fluorescence lifetimes of InP NCs with multilayer shells are longer than those with a single shell. For example, the fluorescence lifetime of InP/ZnSeS/ZnS is three times longer than InP/ZnSeS due to the suppression

© 2023 Wiley-VCH GmbH

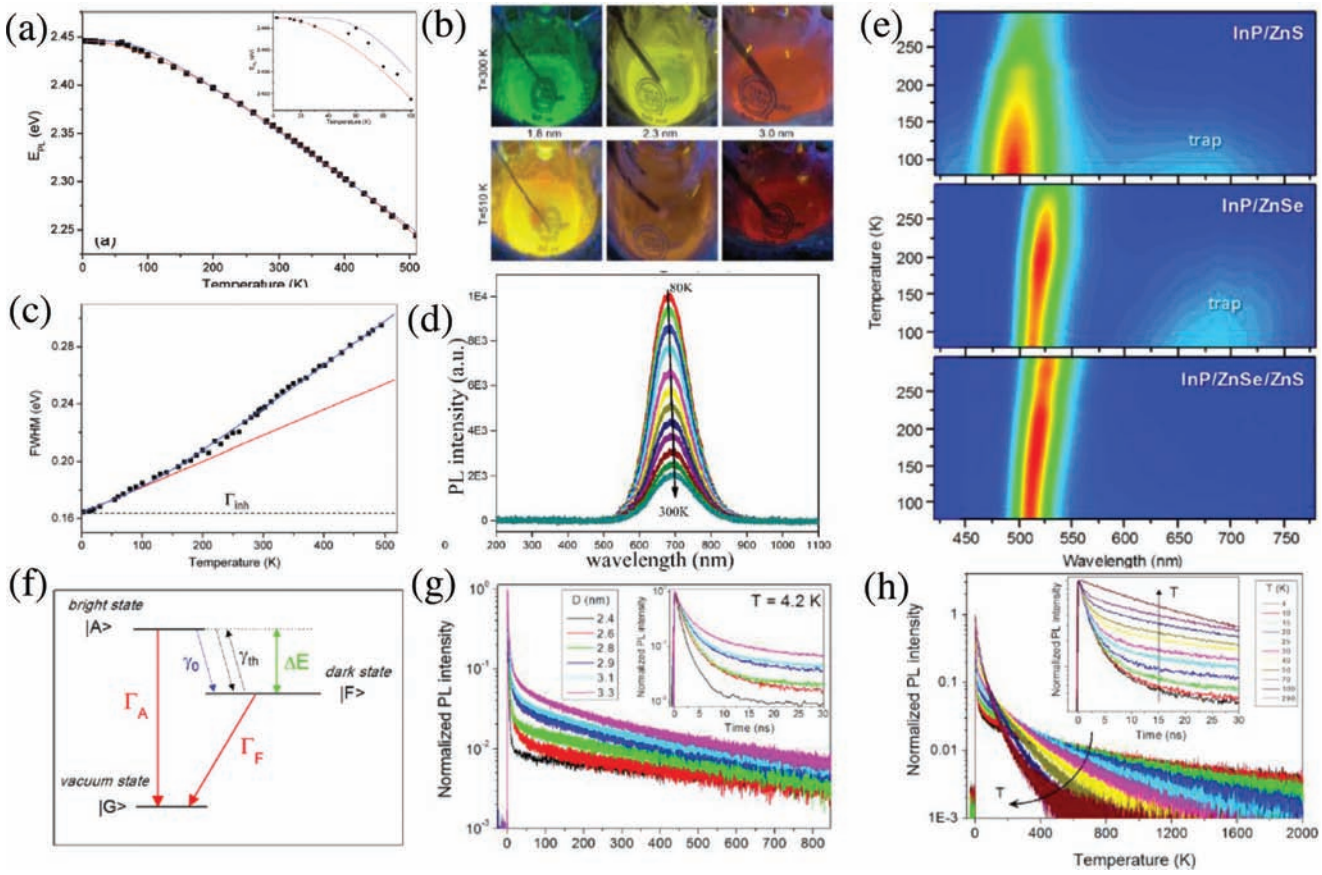

Figure 6. a) Fluorescence peaks of InP/ZnS NCs at 2–525 K. b) Colloidal solutions of InP/ZnS NCs at 300 and 510 K with different InP sizes under UV lamp irradiation. c) FWHM of InP/ZnS NCs at 2–525 K. (a–c) Reproduced with permission.[16] Copyright 200, American Chemical Society. d) Temperature-dependent fluorescence spectra of InP/ZnS NCs at 80–300 K. Reproduced with permission.[11] Copyright 2020, Elsevier. e) InP/ZnS (Top), InP/ZnSe (Medium), InP/ZnSe/ZnS (Bottom) fluorescence pseudocolor map at 80–300 K. Reproduced with permission.[30] Copyright 201, American Chemical Society. f) Schematic diagram of the exciton fine structure of InP/ZnS NCs. g) Fluorescence decay curves of InP/ZnS NCs with InP core sizes from 2.4 to 3.3 nm at 4.2 K. h) The fluorescence decay curves of InP/ZnS NCs with an InP core size of 2. nm ranged from 4 to 20 K. The insets of (g) and (h) show the high-resolution fast-component decay process of InP/ZnS NCs. (f–h) Reproduced with permission.[13] Copyright 2016, American Chemical Society.

of defect-related emission by the ZnS shells.[31] In addition, the fluorescence lifetime of InP/ZnSeS can be slightly adjusted by modulating the ratio between Se and S atoms.[83] As can be seen in Table 1, the fluorescence lifetime of the InP NCs at room temperature is about hundred of nanoseconds. It is found that the fluorescence lifetime of InP NCs increased by an order of magnitude after Cu doping.[83] The dramatical increase of fluorescence lifetime is undoubtedly extremely beneficial for the fluorescence lifetime imaging.[85] Impressively, the fluorescence lifetime of Mn-doped InP/ZnS NCs can reach the order of milliseconds, due to the mechanism of $4T^1$-$6A^1$ transition.[32,33]

The fluorescence decay time of InP NCs also dependents on the environmental temperature. The average fluorescence lifetime of InP NCs increases with the decrease of temperature. In addition, more insightful photophysical properties of InP NCs, such as the fine structure of the emission, can be recorded through the temperature dependence of the PL decay. Normally, the fine structure of NCs involves optically transition-allowed (F = ±1) and optically transition-forbidden states (F = ±2), which are difficult to be measured at room temperature due to the intensive oscillations. However, the apparent separation of these two states can be determined at low temperatures, through the temperature-dependent fluorescence decay measurement (Figure 6f). Recently, the temperature-dependent fluorescence decay of InP/ZnS NCs with InP core of 2.4–3.3 nm and ZnS shell of 2 nm were reported by Bayer et al.[73] As shown in Figure 6g, the InP/ZnS NCs shown size depends fluorescence decay at 4.2 K. Their fluorescence decay consist a fast decay in the nanosecond range and a slow component in hundreds of nanosecond, which are attributed to the bright and dark exciton radiation decay, respectively.[73,86] The former gradually slow down with the increase of core size, while the latter shows opposite trend. Fluorescence decay of InP/ZnS NCs at low temperatures is dominated by dark exciton radiation, because small bright and dark state oscillations lead to reversal of larger numbers of bright excitons to dark ones. Therefore, the fast component decay is also considered as the inversion time from the bright state to the dark one. The temperature-dependent fluorescence decay of InP/ZnS NCs with a core size of 2.9 nm was investigated at 4.2–296 K (Figure 6h). Apparently, the gradual disappearance of the

© 2023 Wiley-VCH GmbH

rapidly decay component with increasing temperature implies a gradual decrease in the number of excitons reversing from the bright to the dark state. However, the long component gradually becomes shorter with increasing temperature as a result of the activation of nonradiative channels in InP/ZnS NCs. The same phenomenon was also observed in the InP/ZnS NCs with core sizes of 2.4–3.3 nm.[87] The separation energy between the bright and dark states can be accessed by fitting the decay rates of the long and short components. As the InP core size increases from 2.4 to 3.3 nm, the separation energy decreases from 16.0 to 5.2 meV. The same trend was confirmed in the study of InP/ZnSe by Brodu et al. Such an energy difference in InP/ZnSe NCs decreases from 7 to 4 meV with the increase of InP core size from 2.9 to 3.6 nm.[87] The discrepancy in the separation energy between InP/ZnS and InP/ZnSe NCs may originate from the difference in the surface defects of InP passivated by ZnSe and ZnS shells. It should be noted that the dark excitons cannot be coupled due to the forbidden transition, but the transition is allowed with the assistance of dangling bonds or phonons of InP, ZnSe, and ZnS.[87,88] Importantly, there is a linear correlation between the recombination lifetime of this dark exciton and the bright-dark separation energy.[73] The same trend has been observed in CdSe NCs, which suggests that InP and CdSe NCs may share the same physical mechanism in terms of exciton fine structure.[89]

3.4. Ultrafast Carrier Dynamics

In order to achieve various optoelectronic devices with better performance based on InP NCs, including LEDs, solar cells, lasers, and detectors, etc.,[3,90,91] the ultrafast carrier dynamic of InP NCs in the femtosecond and picosecond time scales needs to be explored. Extremely fast processes, such as carriers thermalization, carriers cooling, Auger recombination, phonon bottlenecking, and fast defect capturing, occur in the picosecond or even femtosecond range.[92,93] These fast processes play an important role in the radiative recombination of InP NCs. However, conventional steady-state fluorescence and nanosecond-scale transient fluorescence are not sufficient for the study of these carrier dynamics. Therefore, the electron and hole relaxation processes of InP NCs need be deeply analyzed using fs-TAS and fs-TRPL.

As aforementioned, Mandal et al. pointed out that the PLQY of InP/ZnSeS NCs was proportional to the excitation wavelength due to the presence of high-energy defect states which capture carriers under high-energy excitation.[58] To gain a deeper understanding of the underlying mechanism, carriers are excited to different excited states by changing the pump wavelength using ultrafast pump–probe technique.[67] Fitting the exciton bleaching recovery curve gives a fast decay of ≈25 ps attributed to the carrier defect trapping and > 4 ns decay attributed to the band-edge exciton recombination. With the increase of pump wavelength from 430 to 550 nm, the proportion of fast component decreases from 45% to 25%, while the nanosecond component increases from 55% to 75%. As the excitation energy decreases, the number of carriers captured by defects at higher energy levels decreases. As a result, the number of carriers involved in the near-band-edge radiative recombination increases. The same interpretation for the excitation wavelength-dependent PLQY in the InP/ZnS NCs was proposed by Feldmann et al.[94] The time for hot carriers to be captured by high-energy defect states was subsequently determined to be ≈700 fs. The hot carrier cooling time of InP/ZnSeS NCs from the high energy level to the lowest excited state decreases from 220 to 102 fs with the increase of excitation wavelength from 430 to 550 nm. Although the cooling rate of carriers excited at high energies is slow, it increases the chance that the carriers to be captured by the high-energy defect states. Sharper results are shown in the 100 s ultrasensitive single-particle blinking, where the on-duration increases from 6 to 16 s, while the off-duration is reduced from 11 to 5 s under 405 and 568 nm excitation, respectively. Meanwhile, the exciton degeneracy/defect ratio increases from 0.5 to 3.[67]

In order to understand more clearly about the carrier relaxation in InP NCs, the electron and hole relaxation processes are carefully studied. In general, due to the higher electrons□density of state, fast hole relaxation and slow electron relaxation due to phonon bottleneck effect are observed in CdSe NCs. However, different with CdSe NCs, fast electron and slow hole relaxation processes are found for InP NCs.[94] As shown in **Figure 7**a,b, under 600 nm excitation, InP/ZnS NCs exhibit two bleaching signals at 540 and 600 nm, respectively. The bleaching signal at 540 nm is considered as $1S_e$-$1S_{lh/Soh}$ filling, while the signal at 600 nm is considered to be $1S_e$-$1S_{hh}$ filling (Figure 7c). Both of them have the same relaxation time of ≈200 fs, which is comparable to the carrier cooling timescale proposed by Mandal et al.[67] The same relaxation time can be obtained under 525 nm excitation (Figure 7e,f). Due to the higher excitation photon energy (525 nm) relative to 600 nm, the hole is excited to the $1S_{lh/Soh}$ state followed by relaxation to the $1S_{hh}$ state (the red arrow in Figure 7g), resulting in the difference between the orange rising curves in Figure 7b,f.[94] For the case of excess energy excitation at 400 nm, the electron and hole filling times for $1S_e$-$1S_{hh}$ are around 230 and 600 fs, respectively (Figure 7i). The excess energy of electrons is transferred to holes through Auger-like effect, leading to fast electron but slow hole relaxation. Moreover, as schematically shown in Figure 7d, the hole relaxation may also be slowed down by defects states above $1S_{hh}$. It is consistent with the excitation wavelength-dependent PLQY summarized above.[58,67] For the relaxation processes happen in ZnS and ZnSe shells, the carriers can be excited to the ZnSe shell layer but not to the ZnS shell layer under 400 nm excitation. As a result, the InP/ZnSe NCs exhibit slow electron relaxation time (510 fs) than that of InP/ZnS NCs (200 fs) due to electron wave function extending to the ZnSe shell. However, the hole relaxation time of InP/ZnSe (8.8 ps) is an order of magnitude larger than that of InP/ZnS (600 fs), which is ascribed to the small overlap of the electron–hole wave function in the former that slows down the hole relaxation.[94] The same result had been found in the carrier relaxation dynamics for the InP/ZnSe/ZnS NCs studied by Kim et al. In their study, the exciton bleaching recovery curves of InP/ZnSe/ZnS NCs with three different ZnSe interlayer thicknesses were fitted biexponentially, as sketched in Figure 7j.[95] The short and long components correspond to the electron and hole relaxation times, respectively. The short component increases from 340 to 770 fs while the long component increases from 1.6 to 3.3 ps when the ZnSe thickness increases from 1.8 to 3.5 nm. Apparently, both the carrier relaxation rate and the electron–hole wave function overlap were affected by the thickness increase of ZnSe, which results in more electron

© 2023 Wiley-VCH GmbH

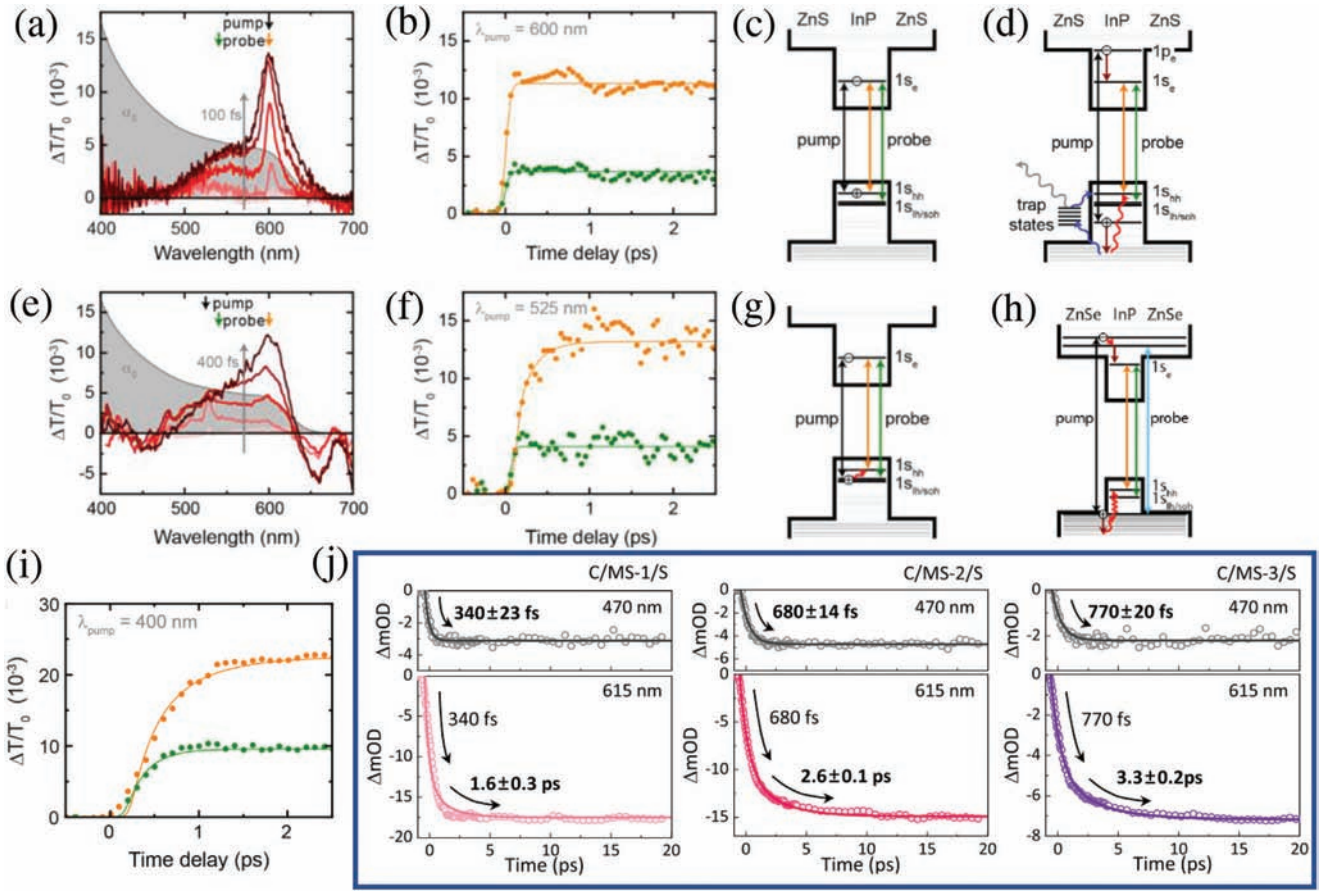

Figure 8. a) TAS spectra of InP/ZnS NCs pumped at 600 nm, the gray area represents the steady-state absorption of InP/ZnS NCs. b) Ground-state bleaching recovery curves of InP/ZnS NCs at 540 and 600 nm in the 2.5 ps range. c,d) Schematic diagrams of the carrier relaxation process of InP/ZnS NCs pumped at 600 and 400 nm, respectively. e) TAS spectra of InP/ZnS NCs pumped at 525 nm. The gray area represents the steady-state absorption of InP/ZnS NCs. f) Ground-state bleaching recovery curves in the 2.5 ps range of InP/ZnS NCs, which are pumped at 525 nm and probed at 540 and 600 nm, respectively. g) Schematic diagrams for the carrier relaxation process of InP/ZnS NCs pumped at 525 nm. h) Schematic illustration for the carrier relaxation process of InP/ZnSe NCs from ZnSe shell to InP. i) Ground-state bleaching recovery curves in the 2.5 ps range of InP/ZnS NCs, which are pumped at 400 nm and probed at 540 and 600 nm. (a–i) Reproduced with permission.[104] Copyright 2016, American Chemical Society. j) Ground-state bleaching recovery curves of InP/ZnSe/ZnS NCs with different ZnSe interlayers probed at 400 nm (Top) and 615 nm (Bottom). Reproduced with permission.[105] Copyright 2021, American Chemical Society.

wave function extended to the ZnSe intermediate layer. Besides, a recent study by Kelley et al. shows that the hole relaxation not only depends on the core size of the InP, but also the excitation energy. With a fixed ZnSe thickness, the energy band offset between InP and ZnSe decreases with the decrease of InP size, leading to an increase of electron wave function present in ZnSe, and therefore slower hole relaxation.[49] In addition, Kellye et al. propose that hole could be trapped by In ions in ZnSe to slow down the relaxation rate (**Figure 8**a). They found a slow rise time through TRPL in InP/ZnSe/ZnS NCs, as shown in Figure 8b,c. They attribute the difference between TAS and TRPL to slow hole relaxation since the TAS signal originates from conduction band electron filling, whereas TRPL is electron and hole. With the increase of In ion concentration, a slower holes relaxation time is found in InP/ZnSe/ZnS through TRPL.[96] Therefore, it can be summarized that the fast electron and slow hole relaxation is associated with the Auger scattering, the overlapping of the electron–hole wave function of InP, the size of ZnSe and InP, and the trapping induced by In ions high-energy defect states.

Ultrafast carrier relaxation processes in doped InP NCs have also attracted strong research interest. Both Cu-doped InP and InP/ZnSe NCs were found to exhibit three decay channels from their exciton bleaching recovery processes, i.e., $\tau_1 = 7.1$ ps, $\tau_2 = 220$ ps, $\tau_3 = 7.8$ ns for Cu-doped InP and $\tau_1 = 24$ ps, $\tau_2 = 183$ ps, $\tau_3 = 4.6$ ns for Cu-doped InP/ZnSe NCs, respectively. Here τ_1 is attributed to the carrier defect capture process, τ_2 is the carrier Cu charge transfer process, and τ_3 is assigned to the exciton relaxation related process. The charge transfer time of Cu-doped InP is slower than that of Cu-doped InP/ZnSe, because ZnSe plays a role as a barrier to block carrier diffusion which results in more excitons in the InP core and a stronger Cu-exciton coupling strength.[84] The difference in trapping (τ_1) and carrier relaxation (τ_3) can be attributed to the passivation of surface defects and nonradiative recombination by the ZnSe shell. Similarly, the carrier relaxation dynamic of undoped and Mn-doped InP/ZnS

© 2023 Wiley-VCH GmbH

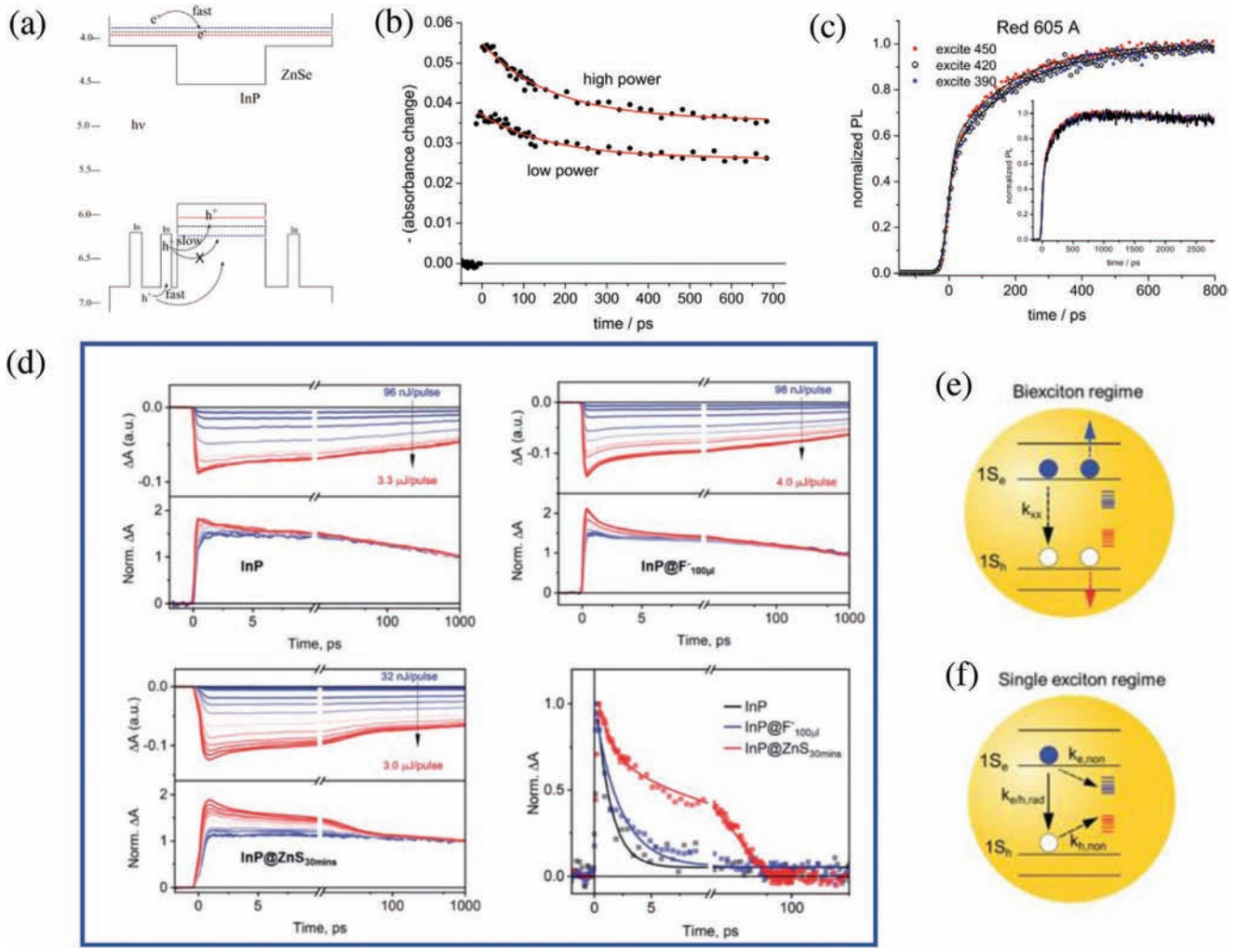

Figure 8. a) Schematic illustration of hole trapping by In ions in the ZnSe interlayer. b) Carrier ground-state bleaching recovery curves (TAS) of InP/ZnSe/ZnS NCs. c) Kinetic curve of InP/ZnSe/ZnS NCs (TRPL). (a–c) Reproduced with permission.[86] Copyright 2021, American Chemical Society. d) Power-dependent ground-state bleaching recovery curves and Auger decay processes of InP, InP@F, and InP@ZnS NCs. e) Schematic diagram of the biexciton photophysical processes. The photogenerated carrier decay through fast nonradiative Auger recombination, where exciton (k_{xx}) excites another electron or hole to higher excited state. f) Schematic diagram of the single exciton photophysical processes. The photogenerated carrier decay through radiative recombination ($k_{e/h,rad}$) and trapping ($k_{e,non}$, $k_{h,non}$) processes. (d–f) Reproduced with permission.[56] Copyright 2020, The Royal Society of Chemistry.

NCs has been studied. It was found that Mn ions can act as energy transfer acceptors leading to an additional 52 ps decay path during the exciton bleaching recovery dynamic.[33]

In addition to the study of carrier relaxation, ultrafast spectroscopy is also beneficial to study the multiexciton effects. The rapid decay of multiple excitons is usually caused by Auger recombination, which greatly increases the laser threshold. LEDs based on semiconductor NCs usually show low EQE due to the nonequilibrium injection of electrons and holes resulting in the Auger effect. The nonradiative Auger recombination is usually caused by the interaction of multiple excitons and is therefore also called a multiexciton Auger recombination. Multiexciton generation usually occurs under high power excitation. For the TAS data of InP/ZnS NCs studied by Lian et al. as shown in Figure 8d, it can be seen that with the increase of excitation power from 0.032 to 3.0 μJ pulse ^{1}, the bleaching signal decays rapidly in early time (≈100 ps) and remains almost unchanged in longer time range (100–1000 ps).[56] The fast decay component is usually attributed to multiexciton Auger recombination (Figure 8e), while the decay process after 100 ps responds to the single-exciton relaxation process (Figure 8f). The highest and lowest excitation powers were normalized at 3 ns, and then the single exciton decay process (low power excitation) was subtracted to obtain Auger lifetimes of around 1, 2.3, and 20 ps for InP, InP@F, and InP/ZnS, respectively.[56] Due to the superior passivation of shell engineering, the Auger lifetime of InP NCs etched by HF is much shorter than that with shell engineering. Moreover, the Auger lifetime of InP NCs is shorter than 1 ps, which were faster than the 10 ps predicted by the universal volume scaling law. However, the Auger lifetime of InP/ZnS was prolonged to 20 ps after the growth of thin ZnS shells. Despite slight electron and hole delocalization to the

© 2023 Wiley-VCH GmbH

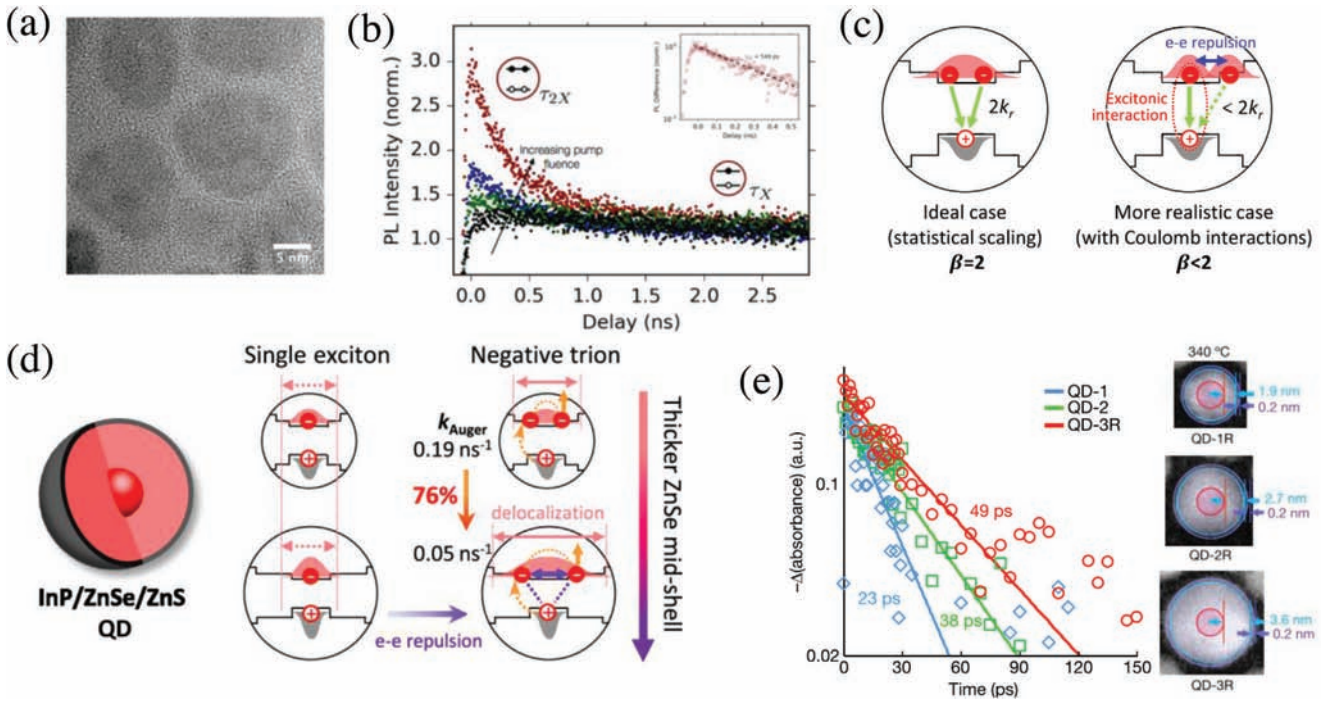

Figure 9. a) TEM image of giant InP/ZnSe NCs. b) Auger decay process of giant InP/ZnSe NCs characterized by TRPL. (a,b) Reproduced with permission.[100] Copyright 2018, American Chemical Society. c) Schematic diagram of the trion delocalization of InP/ZnSe/ZnS NCs to the ZnSe shell. d) Schematic diagram of trion delocalization in ZnSe shell thickness-dependent InP/ZnSe/ZnS NCs. (c,d) Reproduced with permission.[105] Copyright 2021, American Chemical Society. e) Auger lifetimes of InP/ZnSe/ZnS NCs with different ZnSe thicknesses. Reproduced with permission.[60] Copyright 2019, Springer Nature.

ZnS shell layer, the type I electronic band structure of InP/ZnS results in a more than 20-fold increase in the Auger lifetime.[56] It suggests that there may be potential physical mechanisms impacting the Auger recombination process besides reducing the electron–hole wave function overlap.[56] Apart from fs-TAS, fs-TRPL can also be used to probe multiexciton decay process. The excitation power-dependent fluorescence decay process in InP/ZnSe NCs was studied by Reid et al. (**Figure 9**a).[97] The Auger lifetimes of InP/ZnS and InP/ZnSe NCs were determined as 78 and 540 ps, respectively (Figure 9b). The Auger lifetime of InP/ZnS NCs is in the same order of magnitude as that studied by Lian et al. Compared with InP/ZnS NCs, the InP/ZnSe NCs exhibit longer biexciton lifetime as a result of the smaller lattice and conduction band mismatch between InP and ZnSe.[97] The explanation is confirmed by Taehee et al., in which the Auger lifetime of InP/ZnSe/ZnS NCs is related to the ZnSe thickness.[95] The decrease of the Auger decay rate from 0.29 ± 0.13, 0.16 ± 0.11, and 0.10 ± 0.06 ns ^{1} corresponds to ZnSe thicknesses of 1.8, 2.9, and 3.5 nm. In fact, with the thickness increase of ZnSe, the conduction bandgap between InP and ZnSe becomes smaller and more electron wave functions delocalize to the ZnSe shell, thus causing the size-dependent Auger lifetime (Figure 9d).[95] Besides, as the Coulomb interaction of two electrons and one hole in a trion is smaller than that of two electrons and two holes in a biexciton, the weaker binding energy of the trion will lead to the electrons delocalization to a larger shell region, thus slowing down the Auger decay rate (Figure 9c,d). Similar results were observed by Kelley et al.[96] In this work, it was found that the electrons were delocalized to the ZnSe shell due to a small conduction band offset, while the holes were confined in the core due to a large valence band offset. As a result, the negative trion Auger decay depended on ZnSe thickness, while the positive trion Auger decay rate remained constant with the thickness increase of ZnSe.[96] As discussed above, the presence of In ions in the ZnSe layer can trap holes and thus slow down the hole relaxation rate. The biexciton produced by high-energy excitation can form a negative trion after the hole is captured by In ions. Again, since the Coulomb effect of the negative trion is smaller than that of the biexciton, the partial electron wave function extension to ZnSe leads to a thickness dependent Auger lifetime of InP/ZnSe/ZnS NCs. The trion Auger recombination lifetime of 425 ps is much longer than the biexciton lifetime of 80 ps, confirming this explanation. The same trend was confirmed by Jang et al. (Figure 9e).[60] These results suggest that the excess electrons can be controlled to slow down the Auger recombination rate of InP NCs by modulating the ZnSe shell thickness.

3.5. Nonlinear Optical Properties

Compared with CdSe based NCs, InP NCs exhibit lower toxicity. Although the use of heavy metal-free shell coatings such as ZnS and ZnSe can prevent the leakage of Cd elements, the risk of leakage and the incomplete coating of CdSe still make it difficult to achieve commercial applications especially in bioscience. In 2013, Brunetti et al. confirmed that the cytotoxicity of InP/ZnS NCs is much lower than that of CdSe/ZnS NCs.[98] It indicates that InP NCs are more suitable for application in

© 2023 Wiley-VCH GmbH

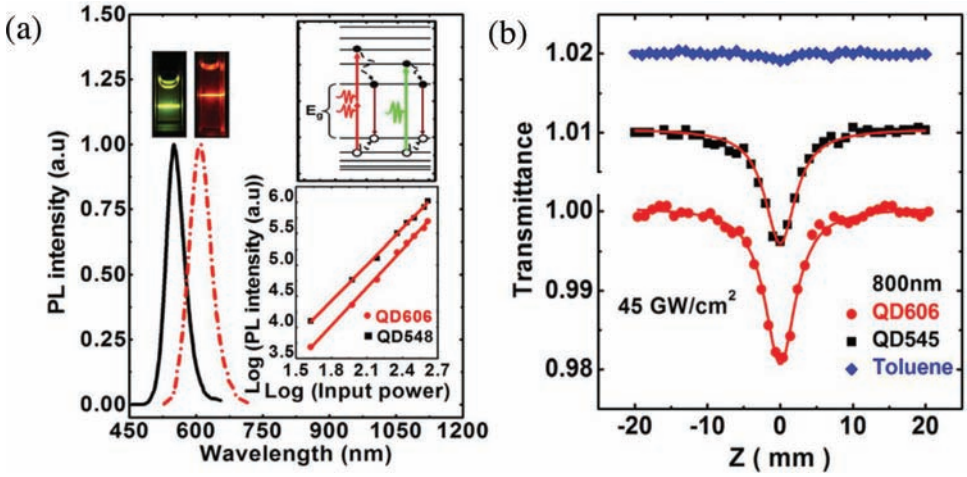

Figure 10. a) Two-photon fluorescence spectra of green and red emitting InP/ZnS NCs. The insets are the power-dependent two-photon fluorescence intensity of InP/ZnS NCs and fluorescence images excited at 800 nm. b) Open aperture Z-Scan curves of InP/ZnS NCs at 800 nm, and the solid line represents the fitted curve. (a,b) Reproduced with permission.[100] Copyright 2013, American Institute of Physics.

biological probes. However, before InP NCs can be applied to bioimaging, the study of their multiphotonic absorption is necessary. Compared to single photon imaging, multiphoton fluorescence imaging has many advantages, such as long penetration depth, excellent signal-to-noise ratio, weak absorption coefficient, and high spatial resolution. In 2005, hydrophilic InP/ZnS core/shell NCs encapsulated by folic acid were synthesized by Prasad et al. The InP/ZnS NCs with a maximum two-photon absorption (2PA) action cross section of ≈100 GM (1 GM = 1×10^{-50} cm^4 s photon $^{-1}$) exhibited good bioimaging property.[99] In 2013, the maximum 2PA cross section (≈6200 GM) of InP/ZnS NCs was obtained by Wang et al.[100] In general, the value of 2PA cross section can be obtained by two-photon induced fluorescence method and Z-scan technique. The mechanism of 2PA can be confirmed by power-dependent two-photon fluorescence. As shown in the inset of **Figure 10**a, the integrated fluorescence intensity of InP/ZnS NCs is quadratic with respect to the excitation power (800 nm), confirming that the fluorescence comes from 2PA rather than the Auger type up-conversion. The 2PA cross sections of green and red InP/ZnS NCs were calculated to be 3500 and 6200 GM, respectively, which are in the same order of magnitude as the red-emitting InP/ZnS (3500 GM) recently studied by Zhang et al.[101] Importantly, these values are comparable to that of CdSe, which suggests that InP NCs may replace CdSe NCs as low toxicity two-photon probes.[102,103] In addition, the red emitting InP NCs exhibit larger multiphoton absorption cross sections because the reduced quantum confinement effect overcomes the increased density of states, in contrast to the observation in ZnS, ZnSe NCs.[104,105] The 2PA cross sections of two InP/ZnS NCs were also acquired by the Z-Scan technique (Figure 10b).[99] Insufficiently, the 2PA cross section of InP/ZnS NCs was only obtained at single-wavelength by Wang et al. The shortcomings were compensated by examining the 2PA cross sections of InP/ZnS NCs with different sizes in the wavelength range from 750 to 900 nm, which were characterized by two-photon induced fluorescence method and Z-Scan technique. The maximum 2PA cross section measured by two-photon induced fluorescence (1300 GM at 850 nm) is smaller than that of Z-Scan (2200 GM at 880 nm), which may be caused by nonradiative paths of absorption or relaxation.[106] Compared to InP NCs that emits visible light, InP that emits at NIR windows has greater potential for application such as bioimaging. Although the NIR emission from InP has been achieved by tuning the electronic structure by Dennis et al., the hundred nanoseconds fluorescence lifetime of the samples is unfavorable for fluorescence lifetime imaging.[59] Fortunately, transition metal doping has been proven to address both needs. For example, we have reported the incorporation of Cu ions to tune the nonlinear optical properties of InP/ZnSe NCs.[84] The Cu-doped InP and Cu-doped InP/ZnSe NCs show emission in the NIR I window (700–1000 nm), with fluorescence lifetimes of 714 and 936 ns, respectively. More importantly, their 2PA cross sections were determined by Z-scan technique in the wavelength range from 970 to 1130 nm, as depicted in **Figure 11**a–d. The maximum 2PA cross sections of Cu-doped InP and Cu-doped InP/ZnSe NCs are 2439 and 10 162 GM at 1030 nm, respectively. Furthermore, their three-photon cross sections in the wavelength range of 1600–2040 nm were determined (Figure 11e–h). The maximum three-photon absorption cross sections of 2.33×10^{-78} and 1.06×10^{-77} cm^6 s^2 photon $^{-2}$ were obtained for Cu-doped InP and Cu-doped InP/ZnSe NCs, respectively. The enhanced multiphoton absorption cross section may be due to the effective surface defects passivation of ZnSe shell, photoinduced internal field shielding, and antenna-like effects.[107] Therefore, InP/ZnSe NCs exhibit comparable multiphoton absorption cross section to those of CdSe and CdTe NCs.

Besides multiphoton absorption, InP NCs also exhibit efficient saturable absorption and nonlinear refraction. For example, Wang et al. have observed the saturable absorption of InP/ZnS NCs under the excitation of femtosecond pulses at 527 nm.[99] In addition, saturable absorption was also observed in InP/ZnS NCs by Kong et al., which were excited by femtosecond pulses at 532 nm (**Figure 12**a).[108] However, InP/ZnS NCs exhibit reverse saturation absorption under 532 nm nanosecond pulses excitation (Figure 12b), which was ascribed to the excited state absorption.[108] In addition, the nonlinear refraction of InP/ZnS NCs excited by femtosecond and nanosecond pulses at 532 nm

© 2023 Wiley-VCH GmbH

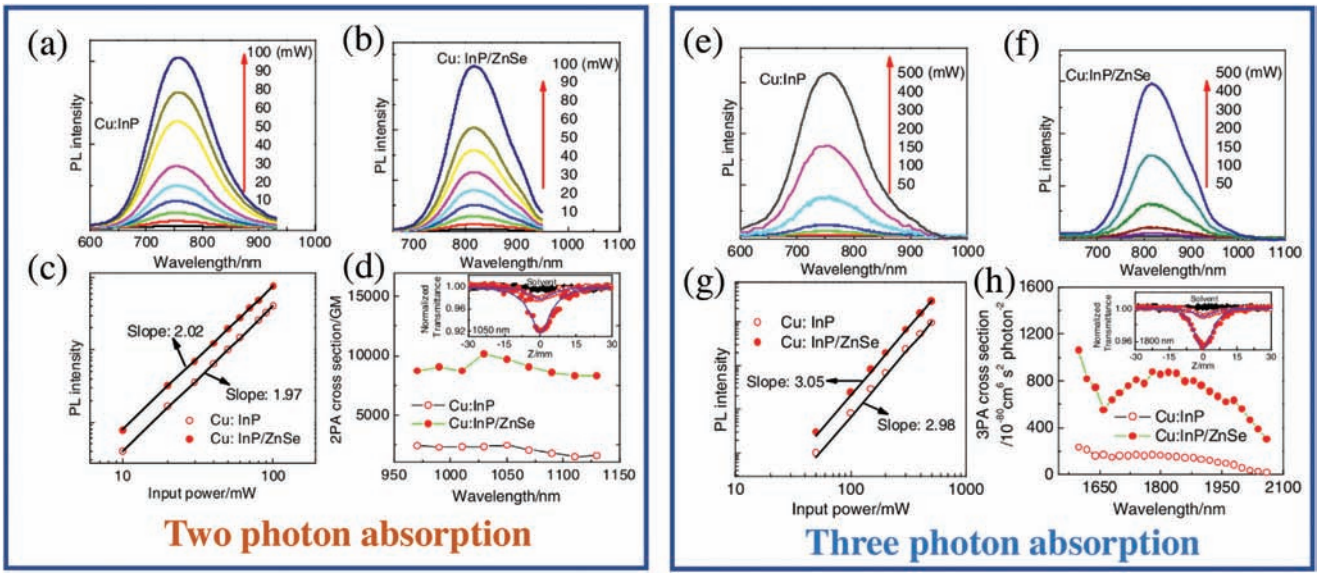

Figure 11. Power-dependent two-photon □uorescence spectra and □uorescence intensity of Cu-doped InP (a) and Cu-doped InP/ZnSe (b). c) Quadratic relationship between power and □uorescence intensity of InP NCs. d) The 2PA cross sections of Cu-doped InP and Cu-doped InP/ZnSe are in the range of □60□1140 nm. Power-dependent three photon □uorescence spectra and □uorescence intensity of Cu-doped InP e) and Cu-doped InP/ZnSe (f). g) Cubic relationship between power and □uorescence intensity of InP NCs. h) The 3PA cross sections of Cu-doped InP and Cu-doped InP/ZnSe are in the range of 1600□2040 nm. (a□h) Reproduced with permission.[84] Copyright 2020, Optical Society of America.

was also studied by Kong et al. Huge differences have been observed in the self-focusing under femtosecond pulse excitation and in the self-scattering under nanosecond pulse excitation depicted in Figure 12c,d, respectively. The self-focusing of InP/ZnS NCs under femtosecond pulse excitation is attributed to the three-term optical Kerr effect of toluene and InP/ZnS NCs electrons. However, the self-scattering focus phenomenon of InP/ZnS NCs under nanosecond excitation is attributed to thermal effects because the pulse duration is close to the electron–hole recombination time.[107] Considering the promising applications in nonlinear optical devices and multiphoton bioimaging demonstrated by InP NCs, it is believed that more attention will be focused on their nonlinear optical studies in future.

4. Applications

4.1. LED

At present, LEDs based on InP NCs have made significant progresses since the first report in 2011.[109] Typically, LEDs are composed of a cathode, a charge transport layer, a charge injection layer, an emission layer, a hole injection layer, a hole transport layer, and an anode. Generally, the efficiency of LED devices can be improved from two aspects. One is the shell engineering to improve the luminescent efficiency and suppress the Auger recombination of active material. The other is the control of electron and hole injection and transport rate to achieve carrier injection balance.[26] InP/ZnSeS NCs were first reported as LED emitting layers in 2011 by Lee et al.[109] However, the poor electron confinement resulted in small EQE (less than 0.1%), as shown in **Figure 13**a. In 2013, high quality InP/ZnSeS LEDs were synthesized by Lim et al., which achieve 3.46% EQE and a maximum brightness of 3900 cd m ^{2} (Figure 13b).[110] The improvement of the LEDs performance is due to the passivation of surface defects of InP by the thick alloy ZnSeS layer. To further enhancing the performance of LEDs, InP/ZnSe/ZnS, and InP/ZnSeS/ZnS NCs with narrow linewidth emission, high PLQY, long Auger lifetime and few surface defects have attracted intensive research interest. In 2018, red-emitting InP/ZnSe/ZnS NCs exhibiting an EQE of 6.6% were reported by Yang et al. The LED device maintained a high EQE in the range of 1–700 cd m ^{2} (Figure 13c).[38] In 2019, no blinking InP/ZnSe/ZnS NCs with a near-unity PLQY were fabricated based on optimized synthesis method by Peng et al.[19] More importantly, LEDs based on high quality InP/ZnSe/ZnS NCs have a maximum brightness over 10 000 cd m ^{2} and a maximum EQE of 12.2%, which exceed those of other Cd/Pb-free LEDs (Figure 13d). In the same year, HF were used to etch InP core by Jang et al. to obtain InP/ZnSe/ZnS NCs.[60] Here the role of HF is to passivate the defects on the surface of InP NCs. Thus, high quality InP/ZnSe/ZnS NCs with an EQE of 21.4% were reported (Figure 13e). The InP/ZnSe/ZnS-based LED has a turn-on voltage of only 1.8 V, a maximum brightness of 100 000 cd m ^{2}, and more importantly, a lifetime of over 1 000 000 h at 100 cd m ^{2}. These extremely superior LEDs are far superior in nature to those Cd-free LEDs and are comparable to the performance of the state-of-the-art Cd/Pb-based LEDs.[60] Although these red-emitting InP-based LEDs have demonstrated competitive capabilities, blue and green-emitting LEDs are lagging behind in performance. In 2019, high-quality green-emitting InP/ZnSeS/ZnS NCs were synthesized by controlling the ratio of halide atoms by Zhang et al.[31] Despite the fact that this InP/ZnSeS/ZnS NCs has a PLQY of 95%, the EQE (7.06%) and other properties of InP/ZnSeS/ZnS based LED are lagging behind those of red LEDs. Recently, the EQE of green InP/ZnSeS/ZnS-based LEDs were further enhanced to 15.2% by HF etching of InP surface defects by Yu et al.[111] For blue LEDs, the synthesis of small

© 2023 Wiley-VCH GmbH

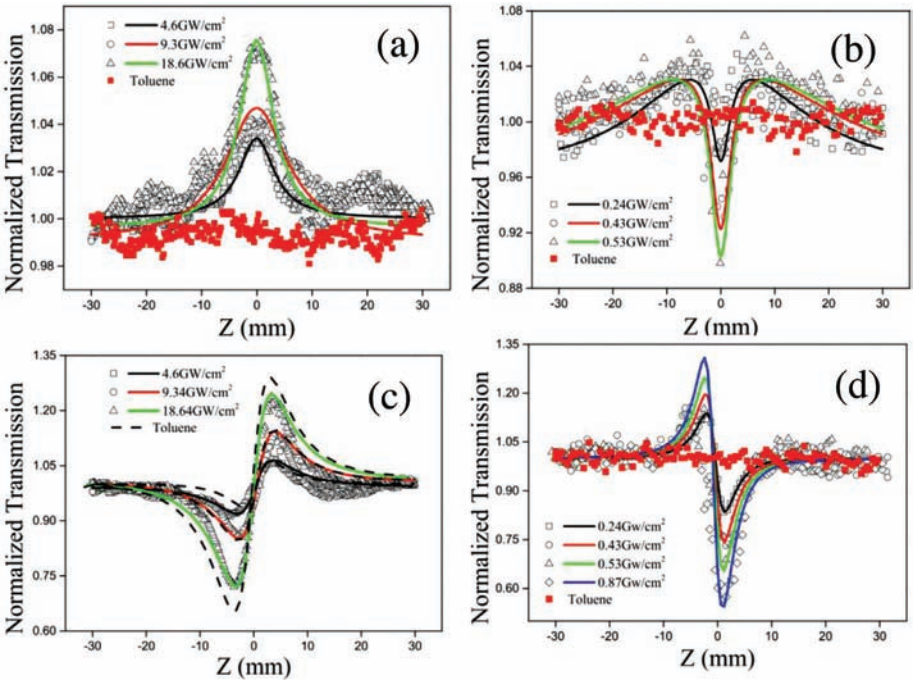

Figure 12. a) Open-aperture Z-Scan curves of InP/ZnS NCs excited by 532 nm femtosecond pulses with di□erent excitation powers. b) Reverse saturable absorption of InP/ZnS NCs excited by 532 nm nanosecond pulses at di□erent excitation powers. c) Self-focusing curves of InP/ZnS NCs excited by 532 nm femtosecond pulses with di□erent excitation powers. d) Self-defocusing curves of InP/ZnS NCs excited by 532 nm nanosecond pulses with di□erent excitation powers. (a□d) Reproduced with permission.[108] Copyright 2018, IOP Publishing Ltd.

size InP NCs cores is difficult due to the high P-source reactivity, which leads to the spectral broadening and low PLQY of InP NCs. In spite of the optical properties being optimized by shell engineering, the small energy band mismatch between ZnSe and InP will induce the extension of electronic wave functions to the ZnSe shell layer, resulting in the fluorescence emission of InP/ZnSe, InP/ZnSeS, InP/ZnSeS/ZnS NCs being difficult to adjust to the blue region. Therefore, the research on high performance blue InP-based LEDs is inadequate. Although InP/ZnS NCs with emission located at 475 nm were applied to the LED emitter layer by Deng et al., the maximum brightness was only 90 cd m ^{2} at a bias voltage of 10 V.[112] It indicates that there is still much space for progress in the research of high-performance blue InP-based LEDs.

Due to the unbalanced injection of electrons and holes which results in a trion Auger recombination, the device emission will be quenched. Many methods have been proposed to control the electron and hole injection rate. In 2017, Mg was added to the charge transport layer (ZnO) by Liu et al. to improve the charge injection efficiency. In their structure as shown in Figure 13f, InP/ZnSeS/ZnS NCs as the green-emitting layer exhibits a brightness of more than 10 000 cd m ^{2} and a turn-on voltage of only 2.2 V.[113] ZnMgO as a charge injection layer can not only enhance the charge balance but also the stability of the device. In 2019, 9-(4-tert-butylphenyl)-3,6-bis(triphenylsilyl)-9H-carbazole (CzSi) incorporated between the InP/ZnSeS NCs and the hole injection layer to control the hole injection rate was proposed by Kwak et al.[114] The schematic structure illustration of this device is presented in Figure 13g. The green-emitting LED combined with the hole suppression layer achieves a maximum current efficiency of 21.6 cd A ^{1} and a maximum brightness of 38 800 cd m ^{2}. Recently, a hole transport material (DOFL-TPD) mixed with InP/ZnSe/ZnS NCs as LED emitting material to achieve uniform films without phase separation was realized by Jang et al. The performance of the LED is enhanced by energy transfer between DOFL-TPD and InP/ZnSe/ZnS NCs.[90] The schematic structure and energy level of this device are shown in Figure 13h,i, respectively. The imbalance injection between electron–hole is suppressed by the high hole mobility and hindered electron leakage to the hole transport layer. The fabricated LED device exhibits an EQE of 18.6% and lifetime over 100 000 h at 100 cd m ^{2}. In addition to controlling the charge injection balance, the incorporation of poly-TPDs between the electron injection layer and the InP/ZnS NCs emission layer to construct white LEDs has been reported by Yang et al.[115] Here the red emission comes from the InP/ZnS NCs, while the blue-green emission comes from the poly-TPD (Figure 13k).

Although these methods have optimized the performance of InP-based LEDs, they are based on the development of Cd/Pb-based LED parameters. The difference in charge injection rates between InP and Cd/Pb-based NCs may cause the performance of InP-based LEDs not to be adequately optimized. Therefore, further research is still needed by changing the type, quality, and structure of the transport layer in the InP-based LED structure.

4.2. Bioimaging

InP NCs have also been found to show important application in fluorescence imaging, due to lower toxicity than the Cd/Pb based

© 2023 Wiley-VCH GmbH

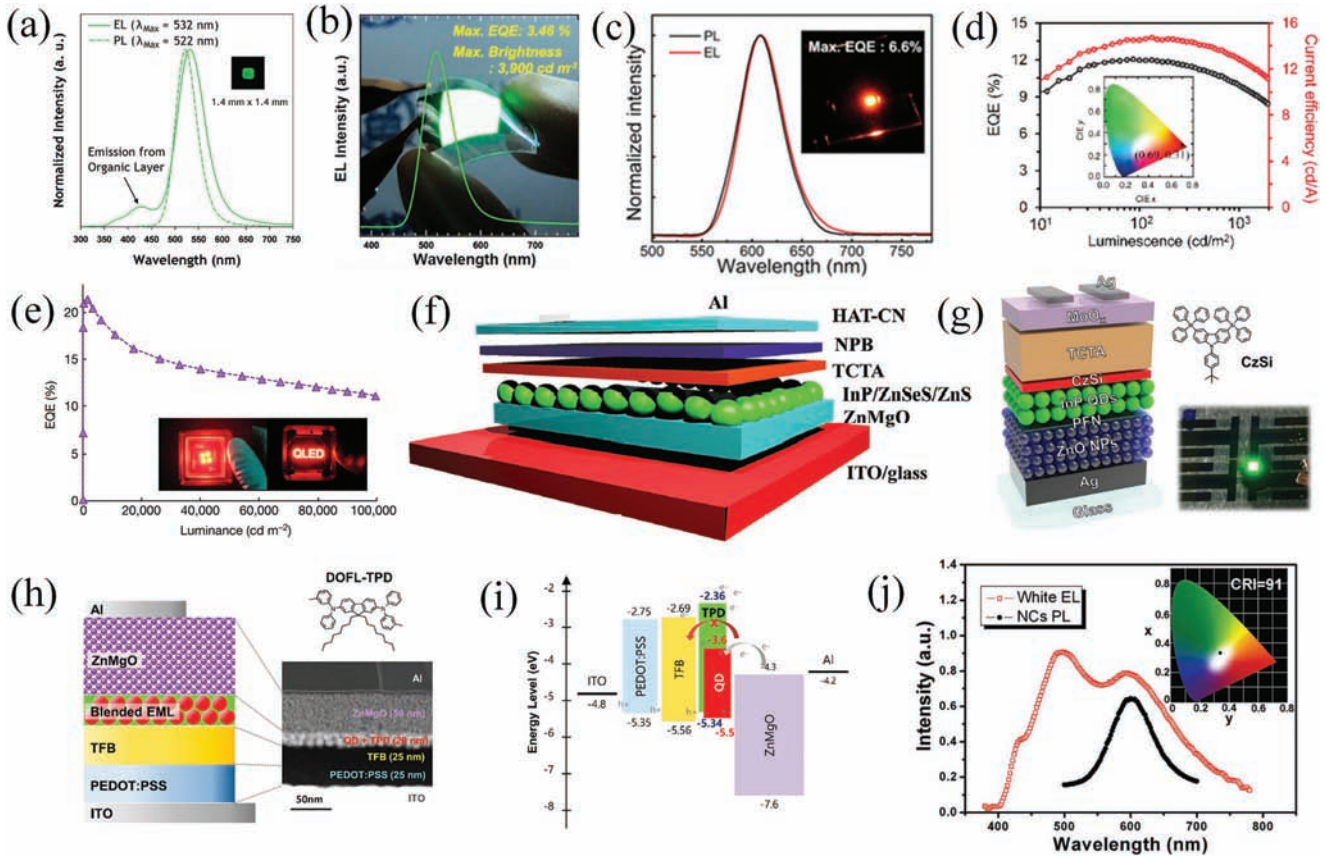

Figure 13. a) PL and electroluminescence spectra of InP/ZnSeS NCs. Inest: the image of InP/ZnSeS-LED. Reproduced with permission.[10□] Copyright 2011, American Chemical Society. b) Electroluminescence spectra and luminescence images of InP/ZnSeS NCs film. Reproduced with permission.[110] Copyright 2013, American Chemical Society. c) PL and electroluminescence spectra of InP/ZnSe/ZnS NCs. Inset: the image of InP/ZnSe/ZnS-LED. Reproduced with permission.[38] Copyright 2018, American Chemical Society. d) EQE and current e□ ciency versus luminance for InP/ZnSe/ZnS NCs-LEDs. Inset: CIE coordinates. Reproduced with permission.[10] Copyright 201□, American Chemical Society. e) Relationship between EQE and luminance of InP/ZnSe/ZnS NCs-LEDs. Inset: InP/ZnSe/ZnS-LED device. Reproduced with permission.[60] Copyright 201□, Springer Nature. f) Schematic diagram of InP/ZnSeS/ZnS-LED structure with Mg in the ZnO electron transport layer. Reproduced with permission.[113] Copyright 201□, Wiley. g) Schematic structure of InP/ZnSeS NCs-LED based on CzSi. Inset: Molecular structure of CzSi and picture of InP/ZnSeS-LED. Reproduced with permission.[114] Copyright 201□, Wiley. h) Schematic structure of DOFL-TPD-based InP/ZnSeS/ZnS-LED. Inset: Schematic of the molecular structure of DOFL-TPD and cross-sectional SEM image of the LED. i) Schematic diagram of the electronic structure of InP/ZnSeS/ZnS-LED based on DOFL-TPD. (h,i) Reproduced with permission.[□0] Copyright 2021, American Chemical Society. j) electroluminescence spectrum of white InP/ZnS-LEDs. Reproduced with permission.[115] Copyright 2012, Wiley.

NCs. To improve biocompatibility, ligand exchange is usually applied to convert oil-soluble InP NCs to water-soluble ones. For the first demonstration of InP/ZnS NCs for fluorescence imaging by Prasad et al., folic acid was used as capping ligands to obtain water-soluble InP/ZnS NCs and the two-photon fluorescence imaging had been achieved as shown in **Figure 14**a.[99] More importantly, water-soluble InP/ZnS NCs were combined with biological antibodies and successfully applied to fluorescent labeling of pancreatic islet cancer cells.[116] It suggests that InP/ZnS NCs have great promise for both fluorescence imaging and fluorescent labeling, especially for early diagnosis of cancer cell. Recently, visible and NIR dual-emitting InP/ZnSe/ZnS NCs were synthesized through a special method proposed by Zhang et al. The former originates from exciton emission, while the latter emission is derived from defect-related emission.[117] Unlike LED applications, the defect emission in InP/ZnSe/ZnS NCs instead of being suppressed. The NIR emission was further enhanced after coating the InP/ZnSe/ZnS NCs with a hydrophilic polymer. Considering the characteristics of longer penetration depth and weaker scattering effect for NIR light, the defect-related emission from InP/ZnSe/ZnS NCs is suitable for applications in bioimaging without doping or size modulation. Therefore, in vitro cellular and in vivo animal imaging was demonstrated by using InP/ZnSe/ZnS NCs as fluorescent probes. As shown in Figure 14b,c, InP/ZnSe/ZnS NCs internalized by cellular tissues under single-wavelength excitation exhibit broadband emission at 550–1000 nm and bright fluorescence imaging. It is mentioned in Section 3.2 that the luminescence of ZnSe/InP/ZnS NCs can be extended to the NIR I window, and such materials also have potential application in fluorescence imaging.[59] The ZnSe/InP/ZnS NCs break the growth bottleneck and achieve maximum exciton emission wavelength up to 845 nm so far. Although the previous InP NCs achieved near-unity PLQY and narrow FWHM (less than 40 nm), the emission wavelength from

© 2023 Wiley-VCH GmbH

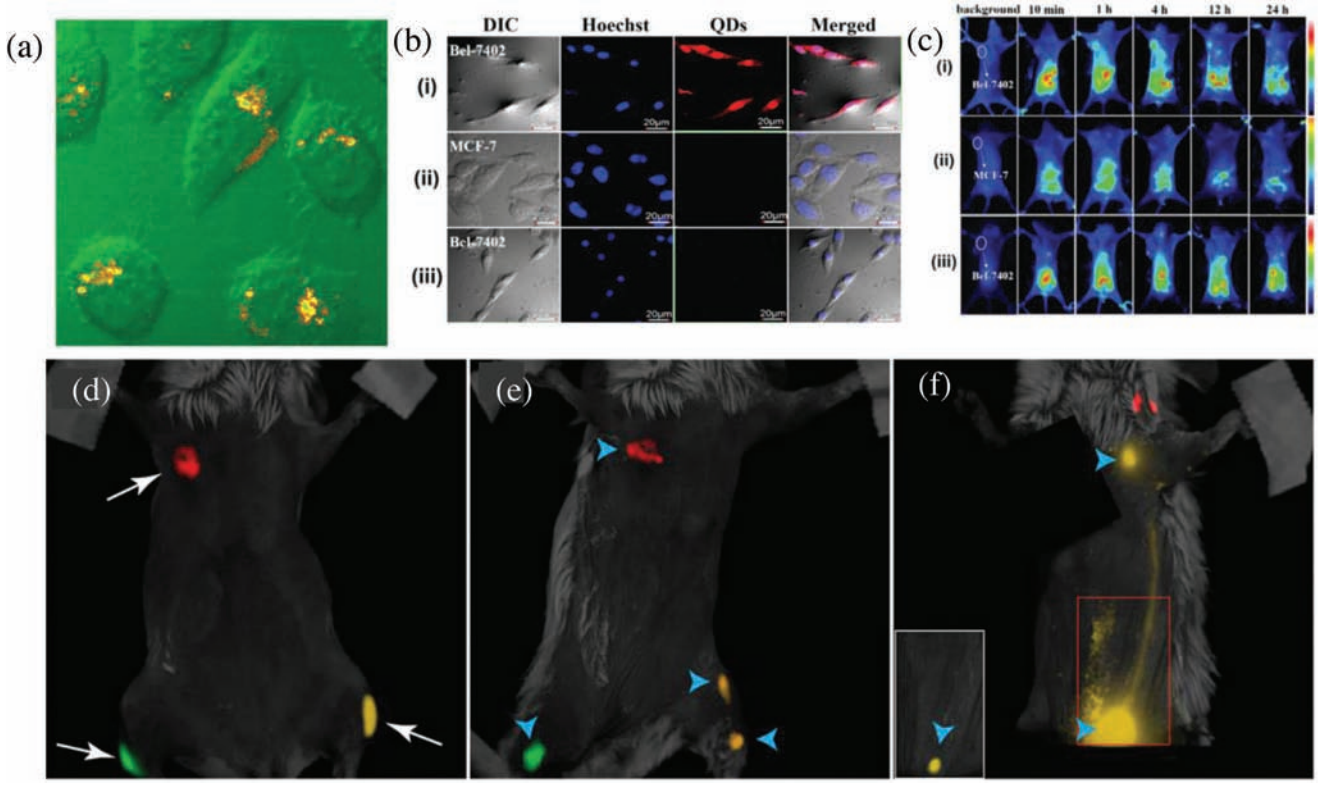

Figure 14. a) Two-photon fluorescence images of human oral epidermoid carcinoma cells treated with InP/ZnS NCs. Reproduced with permission.[88] Copyright 2005, American Chemical Society. b,c) In vitro and In vivo cell imaging of dual-emission InP/ZnSe/ZnS NCs, respectively. Reproduced with permission.[110] Copyright 2010, The Royal Society of Chemistry. Fluorescence imaging maps of QDs650, QDs720, QDs800 at different sites in mice after initial injection of ZnSe/InP/ZnS NCs (d), after 28 min (e), and after 1 h (f). Reproduced with permission.[50] Copyright 2021, American Chemical Society.

InP is all shorter than 750 nm. ZnSe/InP/ZnS NCs were used for in vivo imaging in mice after being coated with a water-soluble polymer. As shown in Figure 14d–f, three ZnSe/InP/ZnS NCs with different emission wavelengths, named QD675, QD720, and QD790, respectively, were injected into different parts of the mice.[59] All of them were drained from the initial injection site to the local lymph nodes 28 min after injection. After 1 h, the local lymph node in the left femoral groin was extended into the collecting duct of the local lymph node in the left axilla, and lymphatic drainage was observed. It suggests that NIR emitting ZnSe/InP/ZnS NCs have promising applications for imaging in living organisms.

4.3. Others

Besides the applications mentioned above, InP NCs can also be used in solar cell due to their high absorption coefficient and narrow bandgap. In 1998, the combination of InP NCs and TiO_2 films was proposed by Zaban et al., producing an 80% photon-to-electron conversion efficiency.[118] In order to further enhance the device efficiency of InP-based solar cells, transition metals including Sn and Cu are doped into InP NCs to control the photon capture efficiency. For example, the synthesized Sn-doped InP NCs were immobilized in TiO_2 films and subsequent ZnS passivation layers were constructed by Lai et al.[119] Compared to undoped InP (**Figure 15**a), a power conversion efficiency (PCE) of 3.5% at AM 1.5G (simulated 1 sun illumination) and a current density of 10.58 mA cm ^{2} was obtained, which confirms that the Sn dopant can enhance the efficiency of the InP-based solar cell. Similarly, the current density of Cu-doped InP/ZnSe (7.4 mA cm ^{2}) was much larger than the undoped ones (4.9 mA cm ^{2}).[120] In contrast to the transition metal doping induced the enhancement of the photovoltaic conversion efficiency, the presence of defects on the surface of InP NCs may limit the mobility of carriers, thus leading to poor photovoltaic efficiency. Houtepen et al. demonstrated that the PCE of InP can be enhanced from 0.65% to 1.17% after adding Zn ions, as a result of the enhanced mobility of surface carriers.[121]

In addition, InP/ZnS NCs have been used for light-driven hydrogen generation, and the schematic diagram of this application is shown in Figure 15b.[122] Similar to the solar cell principle, in order to improve the electron extraction efficiency of InP NCs during photocatalytic process, Cu^{2+} is used as a nonpure energy level to capture holes while p-benzoquinone is used as an acceptor to capture electrons. The rate of electron–hole recombination is slowed down by the Cu-doping while maintaining constant electron extraction efficiency, leading to an increase in the number of extracted electrons and improved efficiency of photocatalytic hydrogen production.

© 2023 Wiley-VCH GmbH

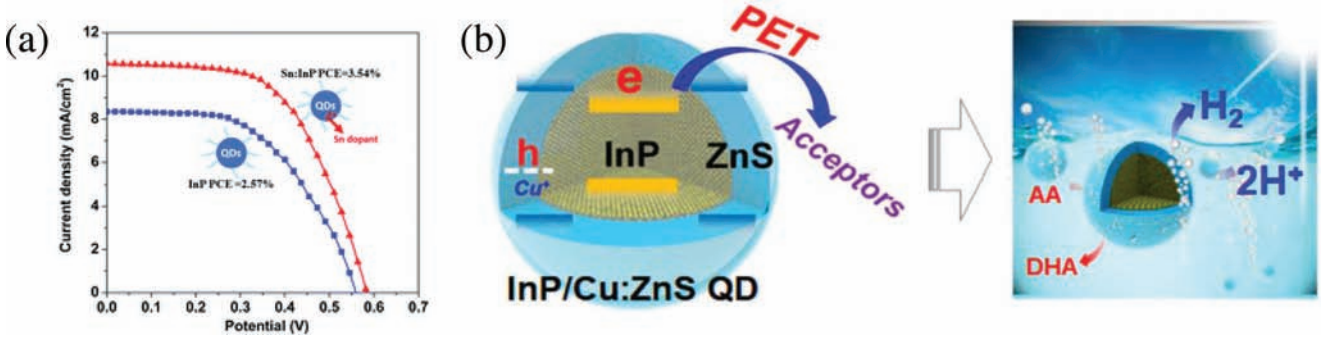

Figure 15. a) *J*–*V* curves and PCE of Sn-doped and undoped InP NCs. Reproduced with permission.[110] Copyright 2015, The Royal Society of Chemistry. b) Charge extraction (Left) and photocatalytic hydrogen production schematic (Right) of Cu-doped InP/ZnS NCs. Reproduced with permission.[122] Copyright 2020, American Chemical Society.

5. Summary and Prospects

In this review, we summarize the synthesis, optical properties and practical applications of InP NCs. In order to obtain high quality InP NCs, a series of exploratory P sources were used. In addition, the optical properties of InP NCs can be optimized by HF etching, ZnE (E = Se/S) shell engineering, ion passivation and doping. Among them, the simplest and most effective method is shell engineering. The optical properties of InP/ZnE and InP/ZnE/ZnE NCs are summarized, including excitation wavelength-dependent PLQY, electron–phonon coupling and fluorescence decay at cryogenic temperatures, electron–hole wave function overlap dependent ultrafast carrier relaxation processes, Auger recombination and nonlinear optical properties. The device efficiency of InP-based LEDs can be regulated through shell and transmission layer engineering. Due to the low toxicity, InP NCs are promising probes for bioimaging application. In addition, InP NCs have also presented great prospects for other applications, such as solar cells and photocatalysis.

Although great progresses have been achieved in the synthesis, optical properties, and applications of InP NCs, challenges and drawbacks still exist. First, the synthesis of small-sized InP NCs with high-efficiency blue emission is difficult due to the high activity of the P source. Therefore, an excellent, cheap, and safe P source may be the focus for synthesizing high-quality InP NCs in the future. Second, generally, the FWHM of InP/ZnSe/ZnS NCs is larger than 35 nm, which may cause poor color purity of the LEDs. Thus, achieving high-quality InP/ZnSe/ZnS NCs is necessary. The exploration of InP nanoplatelets is a promising research direction to improve the color purity and EQE of InP-based LEDs. Third, the extremely fast Auger recombination rate in InP NCs leads to low gain coefficient, posing a huge challenge for commercial application in laser. Possible solutions are also pinned on high-quality InP nanoplatelets. Fourth, the study of the pharmacokinetics of InP NCs also deserves attention due to its weak toxicity to cells. Overall, more efforts need to be paid to realize high-quality InP NCs to avoid heavy metal elements appearing in biological sciences and various excellent optoelectronic devices.

Acknowledgements

H.L. and P.C. contributed equally to this work. The authors acknowledge financial support from the National Natural Science Foundation of China (No. 621□40□□), the Guangdong Basic and Applied Basic Research Foundation (No. 2022A1515011246), and the Science, Technology and Innovation Commission of Shenzhen Municipality (Projects Nos. JCYJ2021032405□441403□, JCYJ20210324120204011, and KQTD20150□1□10313656).

Conflict of Interest

The authors declare no con□ict of interest.

Keywords

bioimaging, InP nanocrystals, light-emitting diodes, optical properties, phosphorus sources

Received: February 1□, 2023
Published online: May 21, 2023

[1] J. M. Pietryga, Y. S. Park, J. Lim, A. F. Fidler, W. K. Bae, S. Brovelli, V. I. Klimov, *Chem. Rev.* **201□**, *11□*, 1051□.
[2] S. Wang, J. Yu, H. Ye, M. Chi, H. Yang, H. Wang, F. Cao, W. Li, L. Kong, L. Wang, R. Chen, X. Yang, *Adv. Opt. Mater.* **2021**, □, 2100068.
[3] G. H. Carey, A. L. Abdelhady, Z. Ning, S. M. Thon, O. M. Bakr, E. H. Sargent, *Chem. Rev.* **2015**, *11□*, 12□32.
[4] Y. Gao, H. Liu, J. Li, X. Deng, W. Hu, S. Xiao, X. Qiu, X. Lin, K. Wang, T. He, *J. Phys. Chem. C* **2020**, *1□□*, □□□4.
[5] W. K. Bae, L. A. Padilha, Y. Park, H. McDaniel, I. Robel, J. M. Pietryga, V. I. Klimov, *ACS Nano* **2013**, □, 3411.
[6] L. E. Brus, *J. Chem. Phys.* **1□□4**, □□, 4403.
[□] T. He, X. Qiu, J. Li, G. Pang, Z. Wu, J. Cheng, Z. Zhou, J. Hao, H. Liu, Y. Ni, L. Li, X. Lin, W. Hu, K. Wang, R. Chen, *Nanoscale* **201□**, *11*, 15245.
[8] L. N. Kolone, *Cancer* **1□□□**, □□, 1□82.
[□] L. Jarup, *Br. Med. Bull.* **2003**, □□, 16□.
[10] L. Li, A. Pandey, D. J. Werder, B. P. Khanal, J. M. Pietryga, V. I. Klimov, *J. Am. Chem. Soc.* **2011**, *1□□*, 11□6.
[11] B. Zhang, Z. Wei, X. Wang, X. Fang, D. Wang, X. Gao, D. Fang, X. Wang, R. Chen, *Nanoscale Res. Lett.* **201□**, *1□*, 36□.
[12] Y. Gao, H. Liu, J. Li, S. Xiao, Z. Guo, R. Pan, X. Lin, T. He, *J. Phys. D* **2020**, □□, 255103.
[13] P. Ramasamy, N. Kim, Y.-S. Kang, O. Ramirez, J.-S. Lee, *Chem. Mater.* **201□**, □□, 68□3.
[14] O. I. Micic, C. J. Curtis, K. M. Jones, J. R. Sprague, A. J. Nozik, *J. Phys. Chem.* **1□□4**, □□, 4□66.
[15] E. Bang, Y. Choi, J. Cho, Y.-H. Suh, H. W. Ban, J. S. Son, J. Park, *Chem. Mater.* **201□**, □□, 4236.

© 2023 Wiley-VCH GmbH

[16] P. Yu, Y. Shan, S. Cao, Y. Hu, Q. Li, R. Zeng, B. Zou, Y. Wang, J. Zhao, *ACS Energy Lett.* **2021**, □, 26□□.
[1□] L. Li, M. Protière, P. Reiss, *Chem. Mater.* **200□**, □□, 2621.
[18] J. H. Jo, D. Y. Jo, S. W. Choi, S. H. Lee, H. M. Kim, S. Y. Yoon, Y. Kim, J. N. Han, H. Yang, *Adv. Opt. Mater.* **2021**, □, 210042□.
[1□] Y. Li, X. Hou, X. Dai, Z. Yao, L. Lv, Y. Jin, X. Peng, *J. Am. Chem. Soc.* **201□**, *1□1*, 6448.
[20] G. Devatha, S. Roy, A. Rao, A. Mallick, S. Basu, P. P. Pillai, *Chem. Sci.* **201□**, □, 38□□.
[21] J. Wang, Z. Lv, X. Xing, X. Li, Y. Wang, M. Chen, G. Pang, F. Qian, Y. Zhou, S. T. Han, *Adv. Funct. Mater.* **2020**, □□, 1□0□114.
[22] J. Tang, F. Liu, M. Lu, D. Zhao, *Sci. Rep.* **2020**, *1□*, 1806□.
[23] D. H. Kim, C. Wu, D. H. Park, W. K. Kim, H. W. Seo, S. W. Kim, T. W. Kim, *ACS Appl. Mater. Interfaces* **201□**, *1□*, 14843.
[24] T. Kim, S. W. Kim, M. Kang, S.-W. Kim, *J. Phys. Chem. Lett.* **2012**, □, 214.
[25] P. Ramasamy, K.-J. Ko, J.-W. Kang, J.-S. Lee, *Chem. Mater.* **201□**, □□, 3643.
[26] Z. Wu, P. Liu, W. Zhang, K. Wang, X. W. Sun, *ACS Energy Lett.* **2020**, □, 10□5.
[2□] H. B. Jalali, S. Sadeghi, I. B. Dogru Yuksel, A. Onal, S. Nizamoglu, *Nano Res.* **2022**, *1□*, 4468.
[28] X. Jiang, Z. Fan, L. Luo, L. Wang, *Micromachines* **2022**, *1□*, 13050□0□.
[2□] B. Chen, D. Li, F. Wang, *Small* **2020**, *1□*, 2002454.
[30] S. Adam, D. V. Talapin, H. Borchert, A. Lobo, C. McGinley, A. R. de Castro, M. Haase, H. Weller, T. Moller, *J. Chem. Phys.* **2005**, *1□□*, 084□06.
[31] P. Liu, Y. Lou, S. Ding, W. Zhang, Z. Wu, H. Yang, B. Xu, K. Wang, X. W. Sun, *Adv. Funct. Mater.* **2021**, □*1*, 2008453.
[32] G. Zhang, S. Mei, X. Wei, C. Wei, W. Yang, J. Zhu, W. Zhang, R. Guo, *Nanoscale Res. Lett.* **201□**, *1□*, 1□0.
[33] H. Liu, G. Shang, C. Ren, Y. Gao, T. He, *J. Phys. Chem. C* **2021**, *1□□*, 21□48.
[34] S. Yu, X. B. Fan, X. Wang, J. Li, Q. Zhang, A. Xia, S. Wei, L. Z. Wu, Y. Zhou, G. R. Patzke, *Nat. Commun.* **201□**, □, 400□.
[35] Z. Liu, A. Kumbhar, D. Xu, J. Zhang, Z. Sun, J. Fang, *Angew. Chem., Int. Ed. Eng.* **200□**, □□, 3540.
[36] S. Haubold, M. Haase, A. Kornowski, H. Weller, *ChemPhysChem* **2001**, □, 6□451.
[3□] Y. Kim, S. Ham, H. Jang, J. H. Min, H. Chung, J. Lee, D. Kim, E. Jang, *ACS Appl. Nano Mater.* **201□**, □, 14□6.
[38] F. Cao, S. Wang, F. Wang, Q. Wu, D. Zhao, X. Yang, *Chem. Mater.* **201□**, □□, 8002.
[3□] A. Vikram, A. Zahid, S. S. Bhargava, H. Jang, A. Sutrisno, A. Khare, P. Trefonas, M. Shim, P. J. A. Kenis, *ACS Appl. Nano Mater.* **2020**, □, 12325.
[40] R. Xie, X. Peng, *J. Am. Chem. Soc.* **200□**, *1□1*, 10645.
[41] W. Yang, W. Zhang, G. Zhang, J. Zhu, G. He, R. Guo, *Opt. Commun.* **201□**, □*1□*, 46.
[42] M. R. Friedfeld, J. L. Stein, D. A. Johnson, N. Park, N. A. Henry, M. J. Enright, D. Mocatta, B. M. Cossairt, *J. Chem. Phys.* **201□**, *1□1*, 1□4□02.
[43] S. Koh, H. Lee, T. Lee, K. Park, W. J. Kim, D. C. Lee, *J. Chem. Phys.* **201□**, *1□1*, 144□04.
[44] J. Hao, Y. Li, J. Miao, R. Liu, J. Li, H. Liu, Q. Wang, H. Liu, M. H. Delville, T. He, K. Wang, X. Zhu, J. Cheng, *ACS Nano* **2020**, *1□*, 10346.
[45] W.-S. Song, H.-S. Lee, J. C. Lee, D. S. Jang, Y. Choi, M. Choi, H. Yang, *J. Nanopart Res.* **2013**, *1□*, 1□50.
[46] M. D. Tessier, D. Dupont, K. De Nolf, J. De Roo, Z. Hens, *Chem. Mater.* **2015**, □□, 48□3.
[4□] P. Reiss, M. Protiere, L. Li, *Small* **200□**, □, 154.
[48] R. Toufanian, M. Chern, V. H. Kong, A. M. Dennis, *Chem. Mater.* **2021**, □□, 1□64.
[4□] E. Jang, Y. Kim, Y.-H. Won, H. Jang, S.-M. Choi, *ACS Energy Lett.* **2020**, □, 1316.
[50] X. Yuan, S. Ji, M. C. De Siena, L. Fei, Z. Zhao, Y. Wang, H. Li, J. Zhao, D. R. Gamelin, *Chem. Mater.* **201□**, □□, 8003.
[51] Y. C. Pu, H. C. Fan, J. C. Chang, Y. H. Chen, S. W. Tseng, *J. Phys. Chem. Lett.* **2021**, *1□*, □1□4.
[52] H. Fu, A. Zunger, *Phys. Rev. B* **1□□□**, □□, 14□6.
[53] R. Lai, Y. Sang, Y. Zhao, K. Wu, *J. Am. Chem. Soc.* **2020**, *1□□*, 1□825.
[54] O. I. Mic´ic´, A. J. Nozik, *J. Phys. Chem. B* **2002**, *1□□*, 43□0.
[55] T. G. Kim, D. Zherebetskyy, Y. Bekenstein, M. H. Oh, L. W. Wang, E. Jang, A. P. Alivisatos, *ACS Nano* **201□**, *1□*, 1152□.
[56] W. Yang, Y. Yang, A. L. Kaledin, S. He, T. Jin, J. R. McBride, T. Lian, *Chem. Sci.* **2020**, *11*, 5□□□.
[5□] F. Pietra, L. De Trizio, A. W. Hoekstra, N. Renaud, M. Prato, F. C. Grozema, P. J. Baesjou, R. Koole, L. Manna, A. J. Houtepen, *ACS Nano* **201□**, *1□*, 4□54.
[58] D. Roy, S. Ghosh, C. K. De, S. Mukherjee, S. Mandal, P. K. Mandal, *J. Phys. Chem. Lett.* **2022**, *1□*, 2404.
[5□] A. M. Saeboe, A. Y. Nikiforov, R. Toufanian, J. C. Kays, M. Chern, J. P. Casas, K. Han, A. Piryatinski, D. Jones, A. M. Dennis, *Nano Lett.* **2021**, □*1*, 32□1.
[60] Y. H. Won, O. Cho, T. Kim, D. Y. Chung, T. Kim, H. Chung, H. Jang, J. Lee, D. Kim, E. Jang, *Nature* **201□**, □□□, 634.
[61] K. E. Hughes, J. L. Stein, M. R. Friedfeld, B. M. Cossairt, D. R. Gamelin, *ACS Nano* **201□**, *1□*, 141□8.
[62] E. J. McLaurin, L. R. Bradshaw, D. R. Gamelin, *Chem. Mater.* **2013**, □□, 1283.
[63] H. Liu, J. Hao, J. Li, J. Cheng, Y. Gao, X. Lin, K. Wang, T. He, *J. Phys. Chem. C* **2020**, *1□□*, 2□840.
[64] Z. Zheng, T. Zhang, H. Liu, Y. Chen, R. T. K. Kwok, C. Ma, P. Zhang, H. H. Y. Sung, I. D. Williams, J. W. Y. Lam, K. S. Wong, B. Z. Tang, *ACS Nano* **201□**, *1□*, 8145.
[65] A. M. Dennis, M. R. Buck, F. Wang, N. F. Hartmann, S. Majumder, J. L. Casson, J. D. Watt, S. K. Doorn, H. Htoon, M. Sykora, J. A. Hollingsworth, *Adv. Funct. Mater.* **201□**, □□, 180□111.
[66] C. K. De, D. Roy, S. Mandal, P. K. Mandal, *J. Phys. Chem. Lett.* **201□**, *1□*, 4330.
[6□] C. K. De, S. Mandal, D. Roy, S. Ghosh, A. Konar, P. K. Mandal, *J. Phys. Chem. C* **201□**, *1□□*, 28502.
[68] N. J. Freymeyer, M. Sophia, M. Click, K. R. Reid, M. F. Chisholm, C. E. Bradsher, J. R. McBride, S. J. Rosenthal, *J. Chem. Phys.* **2020**, *1□□*, 161104.
[6□] J. Park, Y. H. Won, T. Kim, E. Jang, D. Kim, *Small* **2020**, *1□*, 2002454.
[□0] Y. M. Sung, T. G. Kim, D. J. Yun, M. Lim, D. S. Ko, C. Jung, N. Won, S. Park, W. S. Jeon, H. S. Lee, J. H. Kim, S. Jun, S. Sul, S. Hwang, *Small* **2021**, *1□*, 2102□□2.
[□1] J. Yu, C. Zhang, G. Pang, X. W. Sun, R. Chen, *ACS Appl. Mater. Interfaces* **201□**, *11*, 41821.
[□2] J. Li, Z. Guo, S. Xiao, Y. Tu, T. He, W. Zhang, *Inorg. Chem.* **2022**, □*1*, 4□35.
[□3] L. Biadala, B. Siebers, Y. Beyazit, M. D. Tessier, D. Dupont, Z. Hens, D. R. Yakovlev, M. Bayer, *ACS Nano* **201□**, *1□*, 3356.
[□4] Y. P. Varshin, *Physica* **1□□□**, □□, 14□.
[□5] K. P. O□Donnell, X. Chen, *Appl. Phys. Lett.* **1□□1**, □□, 2□24.
[□6] A. Narayanaswamy, L. F. Feiner, A. Meijerink, P. J. van der Zaag, *ACS Nano* **200□**, □, 253□.
[□□] C. Wang, Q. Wang, Z. Zhou, W. Wu, Z. Chai, Y. Gao, D. Kong, *J Lumin* **2020**, □□□, 11□354.
[□8] A. P. Alivisatos, A. L. Harris, N. J. Levinos, M. L. Steigerwald, L. E. Brus, *J. Chem. Phys.* **1□□□**, □□, 4001.
[□□] A, N., L. F. Feiner, P. J. van der Zaag, *J. Phys. Chem. C* **200□**, *11□*, 6□□5.
[80] S. Schmitt-Rink, D. A. Miller, D. S. Chemla, *Phys. Rev. B: Condens. Matter Mater. Phys.* **1□□□**, □□, 8113.
[81] R. Li, S. Chen, X. Li, G. Yin, Y. Gong, J. Yu, G. Pang, J. Liu, Y. Liu, Z. Ni, L. Zhang, R. Chen, H. L. Wang, *Nanoscale* **2020**, *1□*, 36□2.

 © 2023 Wiley-VCH GmbH

[82] D. Valerini, A. Cretí, M. Lomascolo, L. Manna, R. Cingolani, M. Anni, *Phys. Rev. B* **2005**, *71*, 23540.
[83] J.-H. Jo, D.-Y. Jo, S.-H. Lee, S.-Y. Yoon, H.-B. Lim, B.-J. Lee, Y. R. Do, H. Yang, *ACS Appl. Nano Mater.* **2020**, , 1002.
[84] T. He, H. Liu, J. Li, S. Xiao, W. Hu, X. Qiu, X. Lin, Y. Gao, *Opt. Lett.* **2020**, , 1350.
[85] T. He, C. Ren, Z. Li, S. Xiao, J. Li, X. Lin, C. Ye, J. Zhang, L. Guo, W. Hu, R. Chen, *Appl. Phys. Lett.* **2010**, *11*, 211102.
[86] L. Biadala, F. Liu, M. D. Tessier, D. R. Yakovlev, B. Dubertret, M. Bayer, *Nano Lett.* **2014**, *10*, 1134.
[80] A. Brodu, M. V. Ballottin, J. Buhot, E. J. van Harten, D. Dupont, A. La Porta, P. T. Prins, M. D. Tessier, M. A. M. Versteegh, V. Zwiller, S. Bals, Z. Hens, F. T. Rabouw, P. C. M. Christianen, C. de Mello Donega, D. Vanmaekelbergh, *ACS Photonics* **2010**, , 3353.
[88] A. Brodu, M. V. Ballottin, J. Buhot, D. Dupont, M. Tessier, Z. Hens, F. T. Rabouw, P. C. M. Christianen, C. de Mello Donega, D. Vanmaekelbergh, *Phys. Rev. B* **2020**, *101*, 125413.
[89] L. Biadala, B. Siebers, R. Gomes, Z. Hens, D. R. Yakovlev, M. Bayer, *J. Phys. Chem. C* **2014**, *118*, 22300.
[90] M. G. Han, Y. Lee, H.-i. Kwon, H. Lee, T. Kim, Y.-H. Won, E. Jang, *ACS Energy Lett.* **2021**, , 1500.
[91] S. Gao, C. Zhang, Y. Liu, H. Su, L. Wei, T. Huang, N. Dellas, S. Shang, S. E. Mohney, J. Wang, J. Xu, *Opt. Express* **2011**, *10*, 5528.
[92] M. Li, J. Fu, Q. Xu, T. C. Sum, *Adv. Mater.* **2010**, *71*, 1802486.
[93] N. S. Makarov, S. Guo, O. Isaienko, W. Liu, I. Robel, V. I. Klimov, *Nano Lett.* **2010**, *10*, 2340.
[94] A. F. Richter, M. Binder, B. J. Bohn, N. Grumbach, S. Neyshtadt, A. S. Urban, J. Feldmann, *ACS Nano* **2010**, *10*, 14408.
[95] T. Kim, Y. H. Won, E. Jang, D. Kim, *Nano Lett.* **2021**, *71*, 2111.
[96] A. T. Nguyen, P. Cavanaugh, I. J.-L. Plante, C. Ippen, R. Ma, D. F. Kelley, *J. Phys. Chem. C* **2021**, *100*, 15405.
[90] K. R. Reid, J. R. McBride, N. J. Freymeyer, L. B. Thal, S. J. Rosenthal, *Nano Lett.* **2010**, *10*, 000.
[98] V. Brunetti, H. Chibli, R. Fiammengo, A. Galeone, M. A. Malvindi, G. Vecchio, R. Cingolani, J. L. Nadeau, P. P. Pompa, *Nanoscale* **2013**, , 300.
[99] D. J. Bharali, D. W. Lucey, H. Jayakumar, H. E. Pudavar, P. N. Prasad, *J. Am. Chem. Soc.* **2005**, *100*, 11364.
[100] Y. Wang, X. Yang, T. C. He, Y. Gao, H. V. Demir, X. W. Sun, H. D. Sun, *Appl. Phys. Lett.* **2013**, *100*, 021101.
[101] B. Zhang, X. Wang, D. Wang, J. Tang, X. Fang, D. Fang, X. Wang, R. Chen, T. He, Z. Wei, *J. Phys. Chem. C* **2010**, *100*, 2020.
[102] L. Pan, N. Tamai, K. Kamada, S. Deki, *Appl. Phys. Lett.* **2000**, *71*, 05102.
[103] B. H. Zhu, H. C. Zhang, J. Y. Zhang, Y. P. Cui, Z. Q. Zhou, *Appl. Phys. Lett.* **2011**, , 02108.
[104] H. M. Gong, X. H. Wang, Y. M. Du, Q. Q. Wang, *J. Chem. Phys.* **2000**, *100*, 02400.
[105] A. D. Lad, P. P. Kiran, D. More, G. R. Kumar, S. Mahamuni, *Appl. Phys. Lett.* **2000**, , 043126.
[106] D. Wawrzynczyk, J. Szeremeta, M. Samoc, M. Nyk, *APL Mater.* **2015**, , 116108.
[100] W. Chen, S. Bhaumik, S. A. Veldhuis, G. Xing, Q. Xu, M. Gratzel, S. Mhaisalkar, N. Mathews, T. C. Sum, *Nat. Commun.* **2010**, , 1518.
[108] C. Wang, R. Niu, Z. Zhou, W. Wu, Z. Chai, Y. Song, D. Kong, *Nanotechnology* **2020**, *31*, 135001.
[109] J. Lim, W. K. Bae, D. Lee, M. K. Nam, J. Jung, C. Lee, K. Char, S. Lee, *Chem. Mater.* **2011**, , 445.
[110] J. Lim, M. Park, W. K. Bae, D. Lee, S. Lee, C. Lee, K. Char, *ACS Nano* **2013**, , 001.
[111] P. Yu, S. Cao, Y. Shan, Y. Bi, Y. Hu, R. Zeng, B. Zou, Y. Wang, J. Zhao, *Light Sci Appl* **2022**, *11*, 162.
[112] W. Shen, H. Tang, X. Yang, Z. Cao, T. Cheng, X. Wang, Z. Tan, J. You, Z. Deng, *J. Mater. Chem. C* **2010**, , 8243.
[113] H. C. Wang, H. Zhang, H. Y. Chen, H. C. Yeh, M. R. Tseng, R. J. Chung, S. Chen, R. S. Liu, *Small* **2010**, *10*, 160362.
[114] T. Lee, D. Hahm, K. Kim, W. K. Bae, C. Lee, J. Kwak, *Small* **2010**, *10*, 105162.
[115] X. Yang, D. Zhao, K. S. Leck, S. T. Tan, Y. X. Tang, J. Zhao, H. V. Demir, X. W. Sun, *Adv. Mater.* **2012**, , 4180.
[116] K.-T. Yong, H. Ding, I. Roy, W.-C. Law, E. J. Bergey, A. Maitra, P. N. Prasad, *ACS Nano* **2000**, , 502.
[110] J. Zhang, J. Wang, T. Yan, Y. Peng, D. Xu, D. Deng, *J. Mater. Chem. B* **2010**, , 8152.
[118] A. Zaban, O. I. Mic´ic´, B. A. Gregg, A. J. Nozik, *Langmuir* **1000**, *10*, 3153.
[110] S. Yang, P. Zhao, X. Zhao, L. Qu, X. Lai, *J. Mater. Chem. A* **2015**, , 2122.
[120] H. Zhao, X. Li, M. Cai, C. Liu, Y. You, R. Wang, A. I. Channa, F. Lin, D. Huo, G. Xu, X. Tong, Z. M. Wang, *Adv. Energy Mater.* **2021**, *11*, 2101230.
[121] R. W. Crisp, N. Kirkwood, G. Grimaldi, S. Kinge, L. D. A. Siebbeles, A. J. Houtepen, *ACS Appl. Energy Mater.* **2010**, *1*, 656.
[122] J. Bang, S. Das, E. J. Yu, K. Kim, H. Lim, S. Kim, J. W. Hong, *Nano Lett.* **2020**, , 6263.
[123] A. Cros-Gagneux, F. Delpech, C. Nayral, A. Cornejo, Y. Coppel, B. Chaudre, *J. Am. Chem. Soc.* **2010**, *100*, 1814.
[124] T. R. Kuo, S. T. Hung, Y. T. Lin, T. L. Chou, M. C. Kuo, Y. P. Kuo, C. C. Chen, *Nanoscale Res. Lett.* **2010**, *10*, 53.
[125] V. Chandrasekaran, M. D. Tessier, D. Dupont, P. Geiregat, Z. Hens, E. Brainis, *Nano Lett.* **2010**, *10*, 6104.
[126] W. Zhang, S. Ding, W. Zhuang, D. Wu, P. Liu, X. Qu, H. Liu, H. Yang, Z. Wu, K. Wang, X. W. Sun, *Adv. Funct. Mater.* **2020**, , 2005303.
[120] Z. Sun, Q. Wu, S. Wang, F. Cao, Y. Wang, L. Li, H. Wang, L. Kong, L. Yan, X. Yang, *ACS Appl. Mater. Interfaces* **2022**, *10*, 15401.

Huan Liu received his M.S. degree from the College of Physics and Optoelectronic Engineering at Shenzhen University in 2021. He is currently working toward a joint Ph.D. degree between the Harbin Institute of Technology and Southern University of Science and Technology under the supervision of Prof. Rui Chen. His research interests include the synthesis and photophysical properties of semiconductor nanocrystals.

© 2023 Wiley-VCH GmbH

Peixian Chen received her B.S. degree in polymer material and engineering from Guangdong University of Petrochemical Technology in 2018 and will obtain her M.S. degree in polymer chemistry and physics from Hubei University this year. From September 2021 to February 2023, she was a visiting student in the College of Physics and Optoelectronic Engineering at Shenzhen University. Her research area is focusing on the synthesis and characterization of InP quantum dots.

Yanyan Cui is a postgraduate student in the College of Physics and Optoelectronic Engineering at Shenzhen University under the supervision of Prof. Tingchao He. She obtained her bachelor's degree from Shenzhen University in 2022. She focuses on the synthesis of InP quantum dots and development of their applications in biological science and optoelectronic devices.

Yang Gao received her B.Sc. in chemistry from the University of Science and Technology of China (2008); her master's degree in polymer physics and chemistry from the Shanghai Institute of Organic Chemistry, Chinese Academy of Sciences (2011); and her Ph.D. degree from Nanyang Technology University, Singapore (2016). She joined Shenzhen University as an assistant professor in 201□. Her current research focuses on novel ionic quantum structures, luminescent properties, excited state dynamics, and relevant applications.

Jiaji Cheng received his Ph.D. with distinction from the Université de Bordeaux in 2015 focusing on chiral inorganic assemblies and nanophotonics. Afterward, he was a postdoctoal researcher at the Institut de Chimie de la Matière Condensée de Bordeaux studying hierarchical nanomaterials with chiroptical properties. Then he jointed Hubei University as an associate professor in 201□. He has broad, multidisciplinary interests in nanophotonics, chiral plasmonics, and nonlinear and ultrafast optics in hierarchical chiral nanomaterials.

© 2023 Wiley-VCH GmbH

Tingchao He obtained his Ph.D. in physics from Shanghai Jiao Tong University. Following his Ph.D. studies, he held a research fellow position in Prof. Handong Sun's group at Nanyang Technological University. He is currently a professor of physics at Shenzhen University, where his research is focusing on the spectroscopic properties (ultrafast dynamics, nonlinear optics, and chirality) and application of semiconductor nanocrystals and organic–inorganic hybrid metal halides.

Rui Chen received his Ph.D. degree in applied physics from Nanyang Technological University and in physics from Xiamen University. He is currently working at the Department of Electrical and Electronic Engineering at Southern University of Science and Technology. His research interests include the laser spectroscopy, optical properties of materials, optical microcavity, and micro/nanolasers.

© 2023 Wiley-VCH GmbH